




# Near-infrared light-induced photothermal and immunotherapy system for lung cancer bone metastasis treatment with simultaneous bone repair

Guoqing Zhong<sup>a,c,1</sup>, Yali Miao<sup>b,1</sup>, Jielong Zhou<sup>d,a,c,1</sup>, Yijie He<sup>a,c</sup>, Wenjie Yang<sup>a,c</sup>,  
Chongquan Huang<sup>a,c</sup>, Yunhui Zhang<sup>a,c,d</sup>, Jin Xiao<sup>a,c,\*</sup>, Bingqing Bai<sup>a,d</sup>, Jiaqi Zhou<sup>a,c</sup>,  
Renshan Li<sup>a,c</sup>, Tiantian Wei<sup>a,c</sup>, Yu Zhang<sup>a,c,\*\*\*</sup> , Shi Cheng<sup>a,c,\*</sup>

<sup>a</sup> Department of Orthopedics, Guangdong Provincial People's Hospital, Guangdong Academy of Medical Sciences, Southern Medical University, Guangzhou, 510080, China

<sup>b</sup> School of Chemical Engineering and Technology, Guangdong Industry Polytechnic University, Guangzhou, 510300, China

<sup>c</sup> Guangdong Engineering Technology Research Center of Functional Repair of Bone Defects and Biomaterials, Guangzhou, 510080, China

<sup>d</sup> School of Medicine South China University of Technology, Guangzhou, 510080, China

## ARTICLE INFO

### Keywords:

STING activation  
Photothermal immunotherapy  
Black phosphorus  
Bone metastasis

## ABSTRACT

Approximately half of lung cancer patients experience bone metastasis, leading to bone loss, fracture, and other skeletal-related events. Although immunotherapies have significantly advanced the therapeutic landscape for lung cancer, bone metastases have an immunologically "cold" microenvironment, representing a challenging obstacle when treating lung cancer. The combination of immunotherapy and photothermal therapy (PTT) for treating tumor-induced bone defects holds promise for enhancing the efficacy of local tumor ablation and inhibiting tumor recurrence and metastasis through activating systemic immune responses. Herein, we developed an injectable hydrogel-based photothermal immunotherapy system (BP@Gel-CD[SA] hydrogel) incorporating STING agonists (SA) and black phosphorus nanosheets (BPNSs) for high-efficiency tumor elimination, immune activation, and bone regeneration. The photothermal and photodynamic activities of BPNSs induce hyperthermia and ROS-mediated apoptosis of tumor cells. Meanwhile, SA loaded into the nano-boxes in BP@Gel-CD[SA] hydrogel by host-guest interaction significantly activates the cGAS-STING pathway. It stimulates immunogenic cell death (ICD), synergistically promoting immune cell infiltration. Single-cell RNA sequence analysis confirms the modulation of the tumor microenvironment (TME) through the PTT-mediated ICD effect and the transactivation of the cGAS-STING pathway in immune cells of the TME. More importantly, the system can significantly inhibit the growth of distant tumors via systemic immune activation and elicit long-term immune memory in addition to tumor eradication. In the long term, this hydrogel system can promote the formation of new bone at sites of tumor-induced bone destruction, improving bone strength in the affected area. Collectively, this strategy provides an effective and safe option for treating lung cancer bone metastases.

## 1. Introduction

In 2020, an estimated 2.2 million new cases of lung cancer were diagnosed, resulting in 1.8 million deaths [1]. Lung cancer remains the

leading cause of cancer-related deaths worldwide. Approximately 50 % of lung cancer patients develop bone metastasis, a condition associated with poor survival outcomes. Osteolytic bone metastases represent fatal complications, driving a vicious cycle of dysregulated bone homeostasis

Peer review under the responsibility of editorial board of Bioactive Materials.

\* Corresponding author. Department of Orthopedics, Guangdong Provincial People's Hospital, Guangdong Academy of Medical Sciences, Zhongshan 2nd Road, Guangzhou, Guangdong, China.

\*\* Corresponding author. Department of Orthopedics, Guangdong Provincial People's Hospital, Guangdong Academy of Medical Sciences, Southern Medical University, Guangzhou, 510080, China.

\*\*\* Corresponding author. Department of Orthopedics, Guangdong Provincial People's Hospital, Guangdong Academy of Medical Sciences, Southern Medical University, Guangzhou, 510080, China.

E-mail addresses: [xiaojin@gdph.org.cn](mailto:xiaojin@gdph.org.cn) (J. Xiao), [zhangyu@gdph.org.cn](mailto:zhangyu@gdph.org.cn) (Y. Zhang).

<sup>1</sup> These authors contributed equally.

<https://doi.org/10.1016/j.bioactmat.2025.06.008>

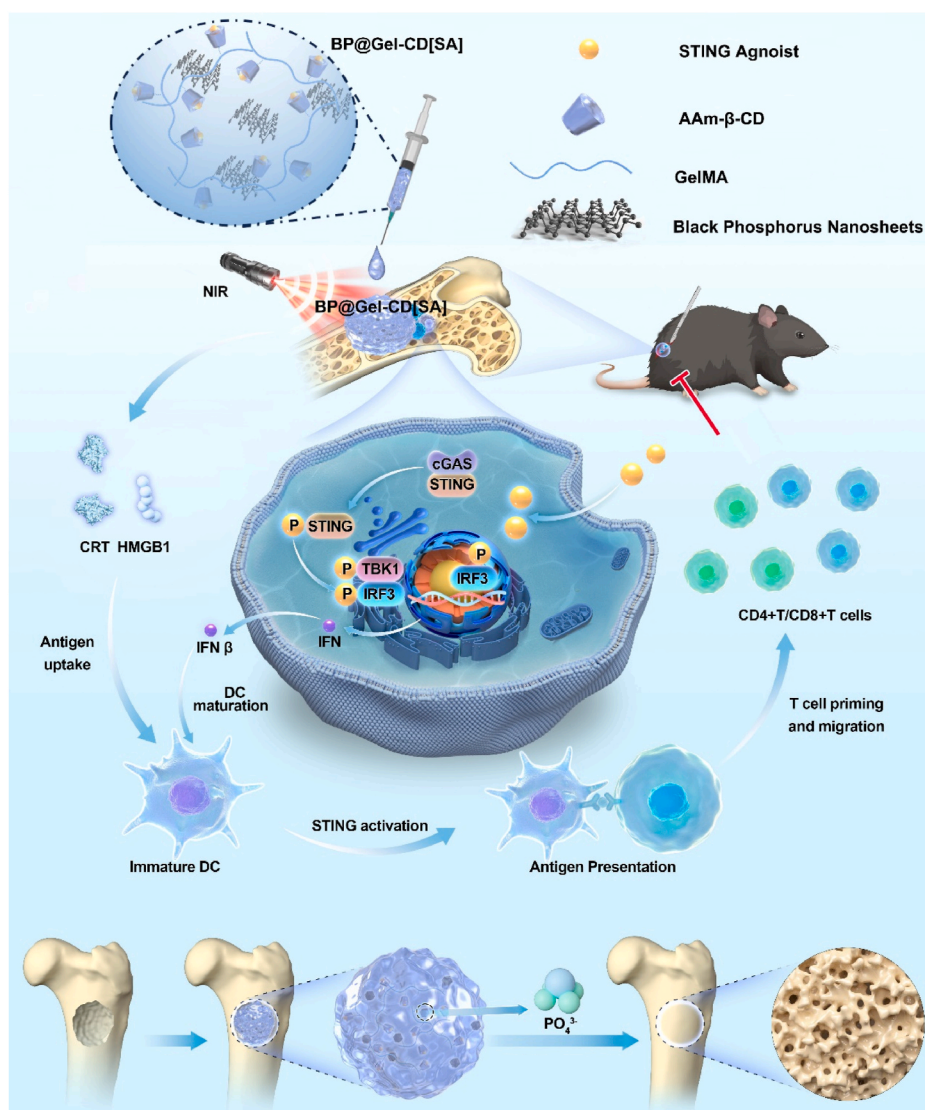
Received 14 April 2025; Received in revised form 27 May 2025; Accepted 3 June 2025

2452-199X/© 2025 The Authors. Publishing services by Elsevier B.V. on behalf of KeAi Communications Co. Ltd. This is an open access article under the CC BY-NC-ND license (<http://creativecommons.org/licenses/by-nc-nd/4.0/>).

and uncontrolled tumor growth. Immune therapies have become the first-line treatment for advanced lung cancer in recent years [2], although their efficacy in treating bone metastases remains limited. Studies indicate that patients with bone metastases often exhibit reduced responses to immune checkpoint inhibitors compared to those with visceral metastases, likely due to the unique characteristics of the bone microenvironment [3]. The 'cold' tumor microenvironment may contribute to the reduced efficacy of immunotherapy in lung cancer patients with bone metastases [4]. Consequently, the development of innovative therapeutic strategies for managing lung cancer derived bone metastases is in need, requiring dual-functional approaches that simultaneously modulate the immunosuppressive tumor microenvironment and facilitate bone regeneration following tumor eradication.

Recent advances in biomedical nanotechnology have introduced novel therapeutic techniques, including photothermal therapy (PTT) and photodynamic therapy (PDT) [5,6]. Phototherapy is a non-invasive cancer treatment method that enables precise control over the irradiation area, minimizing trauma, reducing side effects, and avoiding drug resistance. PTT, which converts light energy into heat, has demonstrated

considerable potential in modulating tumor-suppressive environments. Research suggests that hyperthermia can enhance blood flow within the tumor microenvironment, promoting the infiltration of immune cells, such as tumor-infiltrating lymphocytes, into the tumor [7,8]. This enhanced infiltration boosts the immune response against the "cold" tumor. Moreover, hyperthermia can directly induce tumor cell apoptosis, increasing their susceptibility to immune recognition and elimination. Near-infrared (NIR) light, situated between visible and mid-infrared light in the electromagnetic spectrum, exhibits distinct properties. NIR-II, in particular, offers reduced photon scattering and absorption, lower autofluorescence signals, an enhanced signal-to-noise ratio, superior spatial resolution, and improved tissue penetration. As NIR-II imaging technology and materials science continue to advance, this holds significant promise for tumor diagnosis and therapeutic applications. Studies have demonstrated that NIR-guided PDT and PTT synergistic treatments can lead to complete tumor eradication. Black phosphorus nanosheets (BPNSs) have emerged as efficient photothermal agents, garnering increasing research attention for their application in bone tissue engineering [9]. Furthermore, their degradation products



**Scheme 1.** A diagram illustrating the synthesis (a), and the anti-tumor (b), osteogenic (c) mechanism of BP@Gel-CD[SA] hydrogel treating lung cancer-derived bone metastatic lesions. The photothermal and photodynamic activities of BPNSs can achieve hyperthermia and reactive oxygen species (ROS)-mediated mitochondrial damage, while also enhancing antitumor immunity through immunogenic cell death (ICD). Local application of SA further induces tumor cells to release IFN $\beta$ , which would benefit the recruitment of immature DCs and activation of the adaptive immune system. In the long term, BPNSs can promote new bone formation at tumor-induced bone destruction sites, improving bone strength in the affected area.

consist of inorganic phosphates, which are essential raw materials for bone repair and can serve as mineralizing agents to promote osteogenesis [10].

To optimize the palliative management of bone metastases, it is essential to eliminate residual tumors through PTT and PDT in the short term but also to enhance the local immune microenvironment over the long term. The stimulator of interferon genes (STING) signaling pathway plays a critical role in the innate immune system by promoting the production of type I interferons, which initiate a cascade of reactions that activate immune cells and trigger immune responses [11]. This pathway is of growing importance in cancer therapy, positioning STING agonists (SA) as promising agents for tumor immunotherapy. Research has shown that SA can effectively inhibit various types of murine tumors, with preliminary clinical trials demonstrating their significant anti-tumor potential [12]. To overcome the therapeutic limitations of SA, exploring alternative delivery systems may improve the targeted delivery of these agents to tumors [13]. Moreover, combining SA with other treatments offers a novel approach to anti-tumor therapy.

By combining tumor-targeting and immune-enhancing strategies, this system not only aims to eliminate residual tumors but also to restore bone integrity and mitigate the long-term complications of bone metastasis. Therefore, we designed an injectable multifunctional system (BP@Gel-CD[SA] hydrogel) and explored the synergistic effect of

photothermal therapy (PTT) and immunotherapy on the treatment of tumor-induced bone defects (Scheme 1). The SA encapsulated in nano-boxes through host-guest interaction can effectively induce tumor cells to release IFN $\beta$ . Meanwhile, BPNSs incorporated in this system can achieve hyperthermia and reactive oxygen species (ROS)-mediated mitochondrial damage while enhancing antitumor immunity through ICD. In the long term, this system can not only prevent tumor recurrence and activate a systemic antitumor immune response but also promote the formation of new bone at sites of tumor-induced bone destruction, improving bone strength in the affected area. This represents a multifaceted treatment strategy integrating photothermal, photodynamic, and immunotherapy.

## 2. Results and discussion

### 2.1. Synthesis and Properties of BP@Gel-CD hydrogel with photothermal performance

BPNSs were synthesized using liquid-phase exfoliation from black phosphorus powder (Fig. 1a) and incorporated into hydrogels to form a polymer network with photothermal properties. Transmission electron microscopy (TEM) images revealed the two-dimensional structure of BPNSs, showing an average lateral dimension of approximately 200 nm

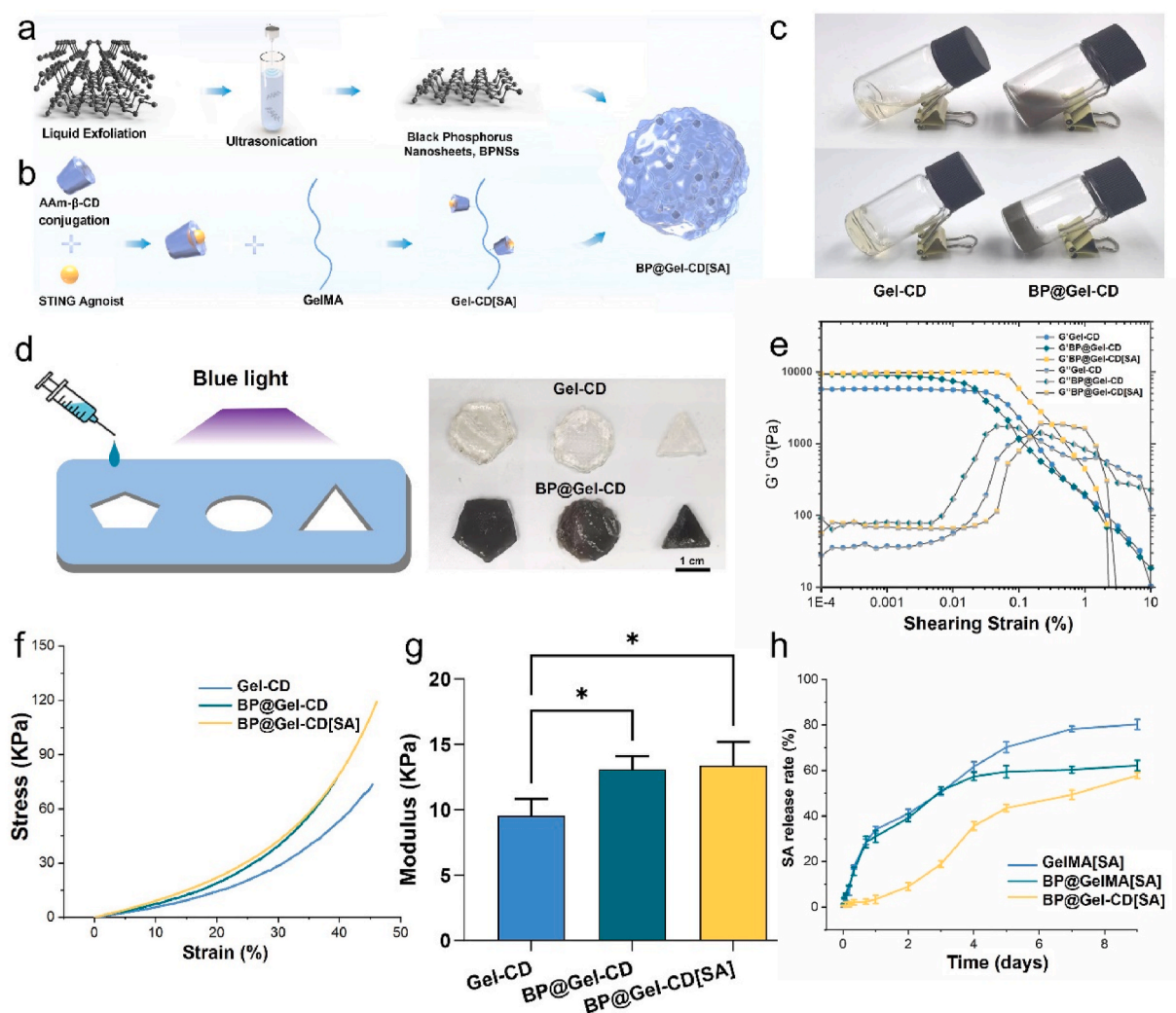


**Fig. 1.** Synthesis and Properties of BP@Gel-CD. (a) Synthesis of black phosphorus nanosheets. (b) Synthesis of BP@Gel-CD. (c) The Gel-CD and BP@Gel-CD hydrogel is cured in 10s under blue light. (d) Various kinds of shapes of the BP@Gel-CD. (e) The change of storage modulus ( $G'$ ) and loss modulus ( $G''$ ) of Gel-CD, BP@Gel-CD, and BP@Gel-CD[SA] hydrogels. (f) Stress-strain curve of hydrogels. (g) Elastic modulus of as-obtained Gel-CD, BP@Gel-CD, and BP@Gel-CD[SA] hydrogels. (h) Quantified drug-releasing process of SA ( $n = 3$ ). Data are presented as mean  $\pm$  SD. \* $p < 0.05$ .



(Fig. S1). High-resolution TEM images confirmed their excellent crystallinity, while selected-area electron diffraction (SAED) patterns validated that the crystalline characteristics were preserved during the exfoliation process. GelMA was covalently crosslinked with AAm- $\beta$ -CD through an amide reaction to form Gel-CD (synthesis pathway shown in Fig. 1b). Subsequently, photopolymerization of AAm- $\beta$ -CD and GelMA, along with BPNs, was conducted to form Gel-CD and BP@Gel-CD hydrogels using lithium phenyl (2,4,6-trimethylbenzoyl) phosphinate (LAP) under blue light exposure (Fig. 1c). Injection of the prepolymer solution into a mold enabled the creation of hydrogels in variable shapes (Fig. 1d), demonstrating excellent shape tunability suitable for filling bone metastasis defects of various geometries.

We further utilized the cavity size properties of  $\beta$ -CD to load SA into the BP@Gel-CD hydrogel, aiming to investigate the synergistic immunological effects of SA.  $^1\text{H}$  NMR spectra showed that, compared to  $\beta$ -CD, acrylamide-modified  $\beta$ -CD (AAm- $\beta$ -CD) exhibited signals at 5.7–6.3 ppm, corresponding to the protons of  $-\text{CH}=\text{CH}_2$  (Fig. S2). Additionally, the signal at 2.1–2.2 ppm, associated with AAm- $\beta$ -CD, shifted and eventually disappeared due to the encapsulation of STING (Fig. S2). These results confirmed the successful conjugation of carbon-carbon double bonds in AAm- $\beta$ -CD and the efficient loading of SA. AAm- $\beta$ -CD loaded with SA was covalently incorporated into the hydrogel network via photopolymerization. The FTIR spectrum (Fig. S3) revealed a prominent  $-\text{NH}_2$  stretching vibration peak at  $3416\text{ cm}^{-1}$  and  $1642\text{ cm}^{-1}$  in the infrared spectrum of  $\beta$ -CD. After acrylamide modification, the  $-\text{NH}_2$  characteristic peak at  $3416\text{ cm}^{-1}$  of  $\beta$ -CD shifted to a lower wavenumber ( $3388\text{ cm}^{-1}$ ), and the peak at  $1642\text{ cm}^{-1}$  broadened significantly. Furthermore, the inclusion of SA caused the disappearance of the characteristic peak of AAm- $\beta$ -CD at  $856\text{ cm}^{-1}$ . Additionally, the  $-\text{CH}_2$  characteristic peak of AAm- $\beta$ -CD, originally at  $2929\text{ cm}^{-1}$ , shifted to a lower wavenumber due to electrostatic and hydrophobic interactions between SA and AAm- $\beta$ -CD. Taken together, these results confirmed the successful conjugation of carbon-carbon double bonds in AAm- $\beta$ -CD and the efficient loading of SA. AAm- $\beta$ -CD loaded with SA was covalently incorporated into the hydrogel network via photopolymerization.

We further conducted rheological measurements and dynamic thermomechanical analysis (DMA) to assess the mechanical properties of BP@Gel-CD[SA] hydrogel. From the oscillatory rheological analysis (Fig. 1e), the linear viscoelastic region of hydrogel was initially determined by detecting the change of storage modulus ( $G'$ ) and loss modulus ( $G''$ ) as a function of shear strain. In the strain range of linear viscoelastic region,  $G'$  and  $G''$  of Gel-CD, BP@Gel-CD and BP@Gel-CD[SA] hydrogels were constant values. However, the  $G'$  values of BP@Gel-CD and BP@Gel-CD[SA] hydrogels were significantly higher than those of Gel-CD, indicating that the introduction of BPNs significantly increased the storage modulus and enhanced the cross-linking network strength. Dynamic thermomechanical analysis (DMA) was employed to characterize the mechanical properties of the hydrogels, with the stress-strain curves depicted in Fig. 1f. The compression modulus of the BP@Gel-CD and BP@Gel-CD[SA] hydrogels exhibited a significant enhancement compared to that of the Gel-CD hydrogel (Fig. 1g). Additionally, SEM images (Fig. S4) showed that the pore structure of the hydrogel became smaller and more compact after the introduction of BPNs. The denser crosslinked network was the main factor contributing to the increased mechanical strength of BP@Gel-CD and BP@Gel-CD[SA] hydrogels. These results thus confirmed the mechanical reinforcement of BPNs in the hydrogels.

The release of SA from the hydrogels was monitored over 10 days (Fig. 1h). On the first day, SA exhibited rapid diffusion with a burst release from GelMA and BP@GelMA hydrogels, whereas BP@Gel-CD hydrogel showed significantly slower release kinetics. By day 4, the cumulative release of SA from GelMA and BP@GelMA hydrogels reached nearly 60 % of the total loaded amount, markedly exceeding that of BP@Gel-CD hydrogel. These findings suggest that the inclusion of  $\beta$ -CD in the hydrogel improves SA retention. Additionally, BP@Gel-CD

hydrogel enabled controlled and sustained release of SA.

## 2.2. Properties of photothermal capability and cytotoxicity

To evaluate the photothermal effect in vitro, Gel-CD hydrogel with or without 200 ppm BPNs was irradiated with an 808 nm laser at a power density of  $1\text{ W/cm}^2$  (Fig. 2a). The hydrogel containing BPNs + NIR exhibited a temperature increase of approximately  $20^\circ\text{C}$  after 6 min of irradiation (Fig. 2b), while the Gel-CD hydrogel without BPNs showed only a  $0.5^\circ\text{C}$  temperature rise. The cytotoxicity of the hydrogel was assessed using the live/dead cell stain calcein-AM and propidium iodide (PI). The proportion of dead cells increased with the duration of NIR exposure (Fig. S5). After 10 min of NIR irradiation ( $1\text{ W/cm}^2$ ), almost all A549 cells treated with BP@Gel-CD hydrogel were dead (stained red) (Fig. S5), while cells exposed to BPNs or laser alone remained viable (stained green), demonstrating the good biocompatibility of BP@Gel-CD (Fig. 2c, single-channel images in Fig. S6). Flow cytometry analysis with V-FITC/PI staining revealed that the apoptosis and necrosis rates of lung cancer cells treated with BP@Gel-CD hydrogel + NIR irradiation (5 min,  $1\text{ W/cm}^2$ ) were significantly higher than those of the other groups (Fig. 2d and f). Furthermore, ROS detection using the DCFDA fluorescent probe showed that the BP@Gel-CD hydrogel + NIR group exhibited the highest fluorescence intensity, indicating its effectiveness in generating ROS within tumor cells (Fig. 2f and g). Collectively, these results demonstrate that BP@Gel-CD hydrogel combined with NIR irradiation possesses significant photothermal capability to induce tumor cell death.

## 2.3. In vitro ICD induction and STING activation of BP@Gel-CD[SA]

The heat generated by photothermal therapy not only induces tumor cell death but also triggers ICD, leading to the release of tumor-associated antigens (TAAs) and enhancing the immunogenicity of the tumor [14,15]. Concurrently, SA activate the STING pathway, further boosting the antigen-presenting capability of dendritic cells (DCs) through both mechanisms [16,17] (Fig. 3a). We assessed the exposure of calreticulin (CRT) and the expression of high mobility group box 1 (HMGB1), both proteins associated with ICD, in LLC cells co-cultured with the hydrogel. Immunofluorescence imaging via confocal laser scanning microscopy (CLSM) and ELISA assays for HMGB1 showed that treatment with BP@Gel-CD hydrogel + NIR irradiation significantly reduced the fluorescence intensity of HMGB1 in the nuclei of LLC cells (Fig. 3b and d) while substantially increased its secretion (Fig. S7) compared to the other groups. Likewise, in the BP@Gel-CD hydrogel + NIR group, CRT fluorescence in LLC cells increased by approximately twofold (Fig. 3c and e), and ATP secretion rose fivefold (Fig. 3f) relative to the non-irradiated control group.

To assess the capability of BP@Gel-CD[SA] on the enhancement of cyclic GMP-AMP synthase (cGAS)-STING pathway, we first examined the expression of phosphorylated STING (p-STING) in LLC cells using immunofluorescence staining [18]. A stronger green fluorescence intensity in the three SA-treated groups (i.e., Gel-CD[SA], BP@Gel-CD [SA], and BP@Gel-CD[SA] hydrogel + NIR) (Fig. 3g). The mean fluorescence intensity (MFI) of these groups being approximately twice that of the other groups (Fig. S8a). Additionally, the MFI in the BP@Gel-CD [SA] hydrogel + NIR group was slightly higher than in the Gel-CD[SA] and BP@Gel-CD[SA] groups (Fig. S8a). We then determined the expression of proteins associated with the STING pathway using Western Blotting. As shown in Fig. 3h and Fig. S8b–d, the levels of phosphorylated IRF3 (p-IRF3), phosphorylated TBK1 (p-TBK1), and p-STING were significantly elevated in the cells treated with Gel-CD[SA], BP@Gel-CD [SA], or BP@Gel-CD[SA] hydrogel + NIR. Importantly, the highest upregulation of these proteins was observed in the BP@Gel-CD[SA] hydrogel + NIR group, consisting with the strongest intensity of p-STING in immunofluorescence staining, likely due to the thermal-induced rapid release of SA. These findings demonstrated that



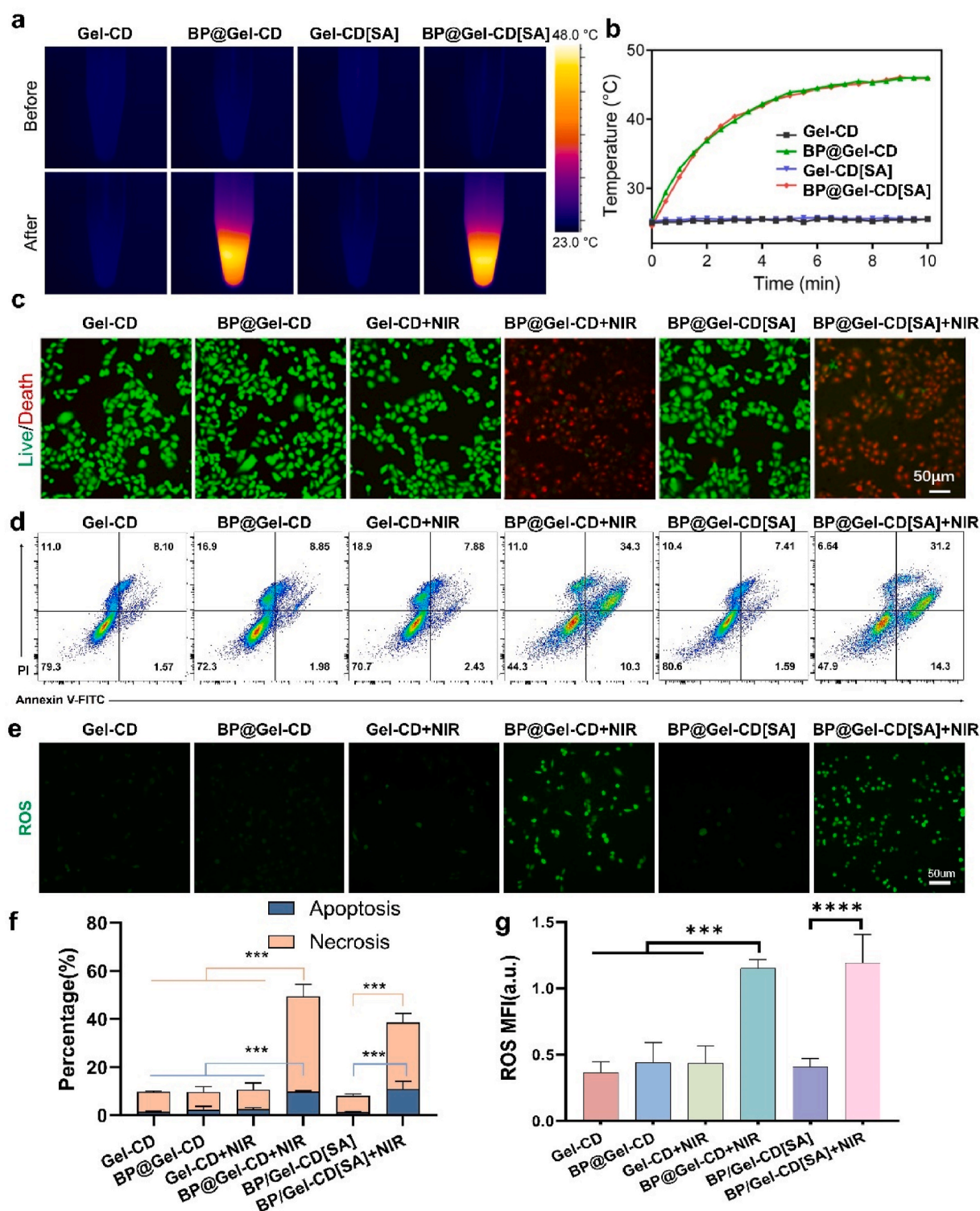


**Fig. 2.** Photothermal transducing capability and cytotoxicity tests in vitro. a) Photothermal conversion tests before and after NIR irradiation in the centrifuge tubes. b) Temperature change curves of hydrogels. c) Cell live/dead staining of each group, scale bars = 50 μm. d) Representative flow cytometry dot plots of Annexin-FITC and PI-stained tumor cells showing apoptosis and necrosis rates after treatments. e) DCFH-DA-based detection of ROS production in LLC cells after the indicated treatments, scale bars = 50 μm. f) The quantification of apoptosis and necrosis rates in the flow cytometry analysis (n = 3). g) Quantification of ROS fluorescence intensity in Fig. 3e (n = 3). Data are presented as mean ± SD. Statistical analysis was performed using one-way ANOVA with Tukey's post-hoc test. \*\*p < 0.01, \*\*\*p < 0.001, \*\*\*\*p < 0.0001.

BP@Gel-CD[SA] hydrogel combined with mild hyperthermia induced by NIR irradiation (5 min, 1 W/cm<sup>2</sup>) can effectively activate the STING pathway. To further evaluate downstream signaling, we measured the secretion of IFN-β, a key effector cytokine induced by STING pathway

activation. As shown in Fig. S9, all three SA-treated groups exhibited a significant increase in IFN-β levels compared to the Gel-CD group, with the BP@Gel-CD[SA] hydrogel + NIR group displaying the highest secretion of IFN-β.

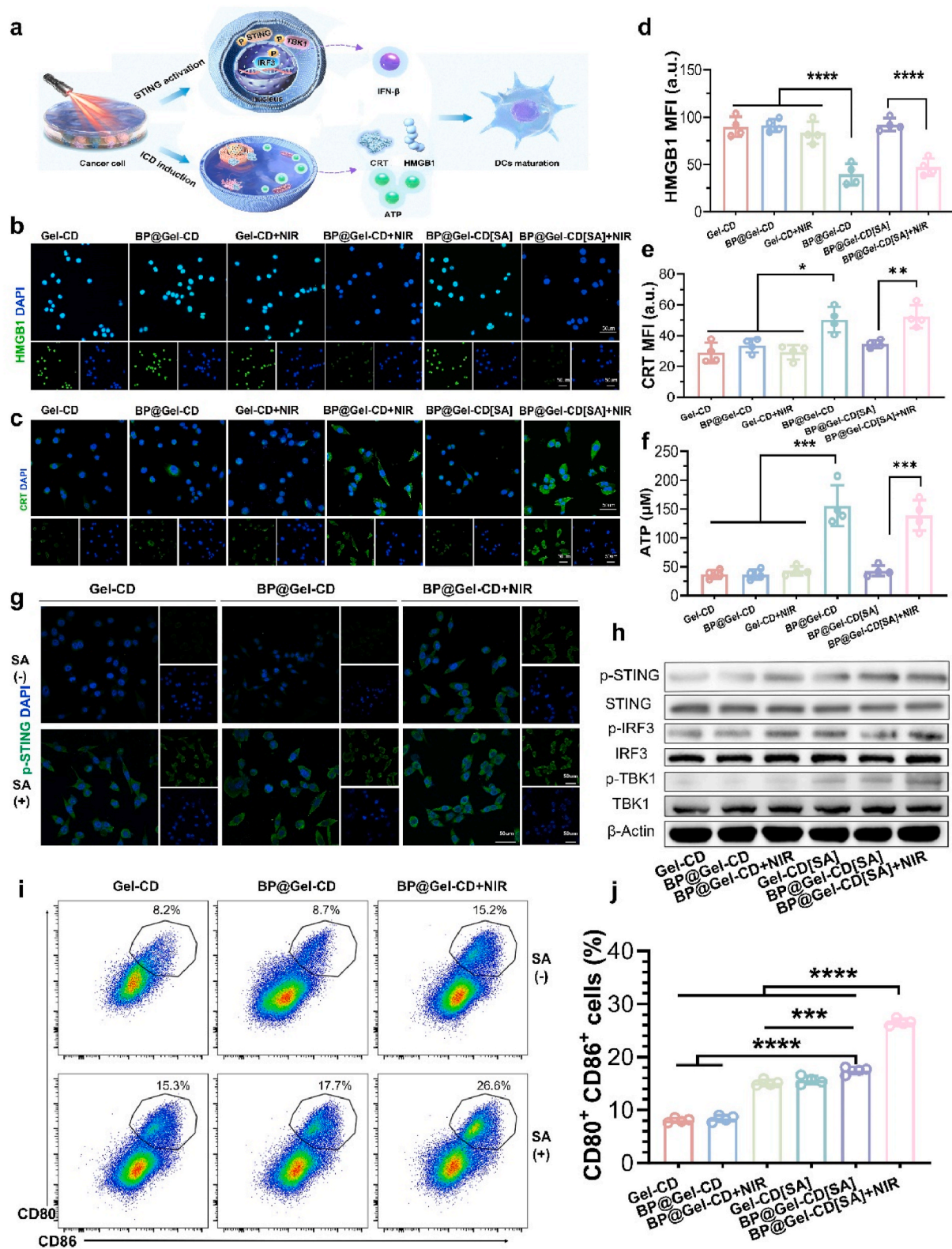


**Fig. 3.** ICD induction and STING activation of BP@Gel-CD[SA] in vitro. **a)** Schematic diagram showing the biological mechanism of DC maturation. **b)** The immunofluorescence captures of HMGB1 in vitro, scale bars = 50  $\mu$ m. **c)** The immunofluorescence captures of CRT in vitro, scale bars = 50  $\mu$ m. Quantification of fluorescence intensity of HMGB1 (**d**) and CRT (**e**). **f)** ATP production assays. **g)** The immunofluorescence captures of p-STING in LLC cells upon treatment of Gel-CD, BP@Gel-CD, BP@Gel-CD + NIR, Gel-CD[SA], BP@Gel-CD[SA] and BP@Gel-CD[SA] + NIR, scale bars = 50  $\mu$ m. **h)** Western blotting showing the levels of STING pathways-related protein in LLC cells upon various treatments. **i)** Flow cytometric profiles and **j)** quantitative analysis of activated DC cells after incubation with LLC cells upon various treatments. Data are presented as mean  $\pm$  SD. Statistical analysis was performed using one-way ANOVA with Tukey's post-hoc test. \*\*p < 0.01, \*\*\*p < 0.001, \*\*\*\*p < 0.0001.



The activation and maturation of antigen-presenting cells are critical for STING-mediated anti-tumor immunity [19]. To assess the effect of BP@Gel-CD[SA] on the maturation of DCs in vitro, we co-cultured LLC cells treated with different hydrogels with mouse bone marrow-derived dendritic cells (BMDCs). Flow cytometry analysis showed that the BP@Gel-CD[SA] hydrogel + NIR group resulted in the highest proportion of CD80+CD86+ mature BMDCs (26.6 %), which was 3.2, 1.7, and 1.5 times higher than the proportions observed in the Gel-CD, BP@Gel-CD hydrogel + NIR, and BP@Gel-CD[SA] treatment groups, respectively (Fig. 3i and j).

These results indicated that BP@Gel-CD[SA] hydrogel combined with NIR irradiation induce immunogenic death and activate the STING pathway, ultimately enhance the maturation of BMDCs.

#### 2.4. The inhibitory effects of hydrogels on tumor recurrence in complete intralesional curettage model of tumor bearing mice

When bone metastases from lung cancer cause discomfort or pose a high risk of pathological fractures, surgical intervention is often required, primarily through complete intralesional curettage [20]. However, the complete intralesional curettage is frequently associated with a high incidence of tumor recurrence. Thus, to approach the clinical manifestation of lung cancer bone metastases after surgical intervention, we established a femoral-transplanted tumor mouse model in C57BL/6J mice and performed complete curettage in tumor site. The therapeutic efficacy in inhibiting tumor recurrence of different treatment groups were subsequently evaluated.

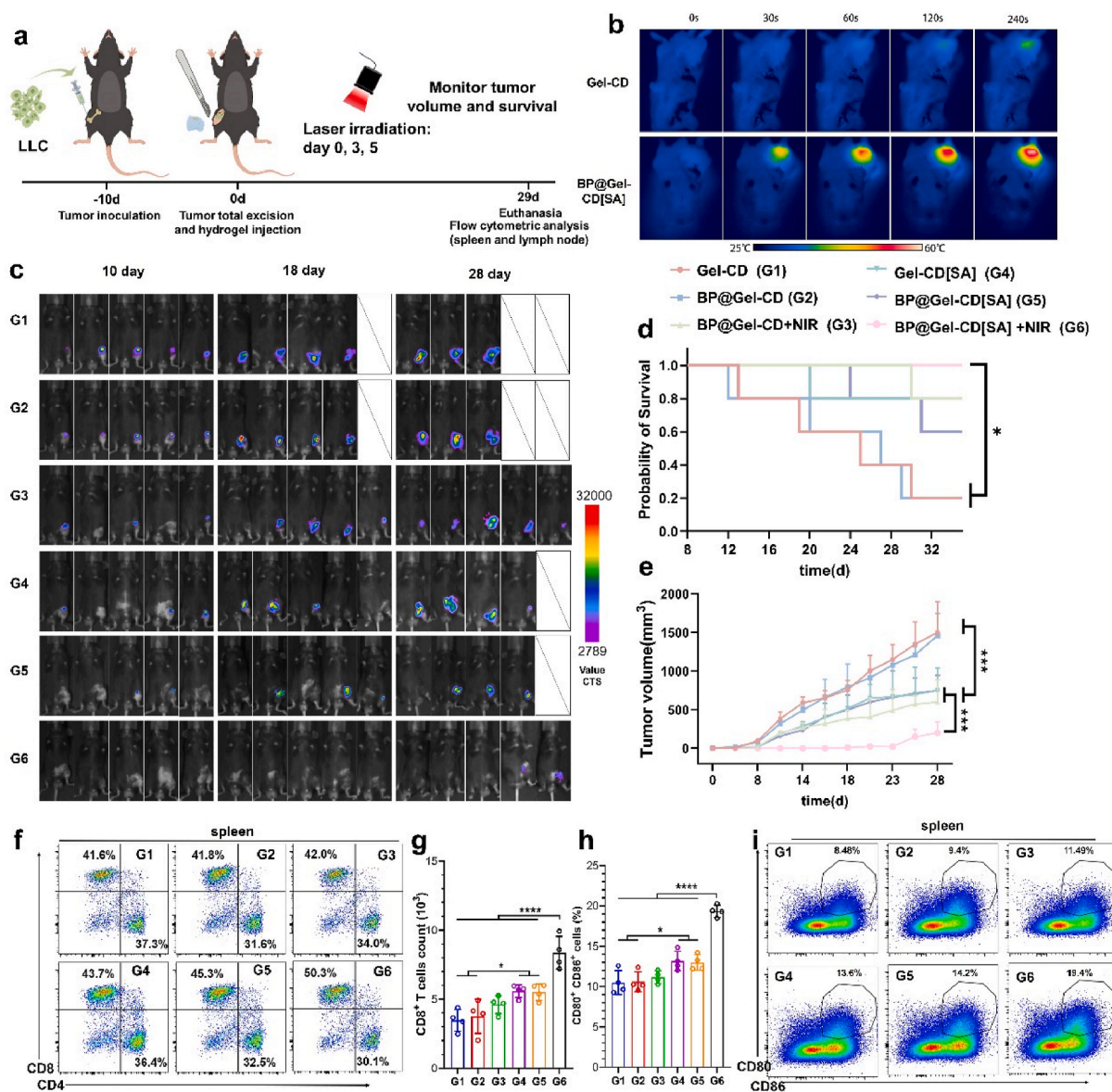


**Fig. 4.** The therapeutic effects of hydrogels on tumor recurrence in complete intralesional curettage model of tumor-bearing mice. a) Timeline schematic for establishing the tumor mouse model and intervention. b) In vivo photothermal conversion ability of the gel under NIR laser at 1 W/cm<sup>2</sup> and 808 nm. c) Representative in vivo imaging system (IVIS) spectrum images in mice from the different treatment groups (n = 5). d) Kaplan-Meier survival analysis in mice from the different treatment groups. The survival curves were statistically tested using the Log-rank test. e) Tumor volume growth curves in vivo (n = 5). Statistical differences in tumor volume between the two groups were analyzed using two-way ANOVA followed by Tukey's post hoc test. f) Representative flow cytometry analysis of the proportion of CD8<sup>+</sup> T cells in the mouse spleen from the different treatment groups. g) Quantitative counts of CD8<sup>+</sup> T cells in the mouse spleen from the different treatment groups. h) Quantitative percentage of CD80<sup>+</sup>CD86<sup>+</sup> DC cells in the mouse spleen from the different treatment groups. i) Representative flow cytometry analysis of the proportion of CD80<sup>+</sup> and CD86<sup>+</sup> in the mouse spleen from the different treatment groups. Data are presented as mean ± SD (n = 4). Statistical analysis was performed using one-way ANOVA with Tukey's post-hoc test. \*P < 0.05, \*\*P < 0.01, \*\*\*P < 0.001, and \*\*\*\*P < 0.0001.



A suspension of  $5 \times 10^5$  luciferin<sup>+</sup> LLC tumor cells was injected into the mouse medial condyle of the femur. After ten days, mice with 50 mm<sup>3</sup> volume of tumor were randomly assigned to six groups (Gel-CD, BP@Gel-CD, BP@Gel-CD + NIR, Gel-CD[SA], BP@Gel-CD[SA], and BP@Gel-CD[SA] + NIR). The femoral LLC tumors were completely curetted, and 50  $\mu$ L of hydrogel was injected into each group. NIR irradiation was applied on the day of surgery (day 0), day 3 and day 5

(Fig. 4a). Compared to Gel-CD, BP@Gel-CD retained high photothermal conversion efficiency after injection into the femoral lesion. Upon irradiation with a 1 W/cm<sup>2</sup> 808 nm laser for 1 min, the temperature exceeded 50 °C, effectively ablating the tumor tissue (Fig. 4b, Fig. S10). In vivo imaging system was used to monitor tumor recurrence. A complete remission rate of 60 % was observed in the BP@Gel-CD[SA] hydrogel + NIR group after 4 weeks, while the Gel-CD and BP@Gel-

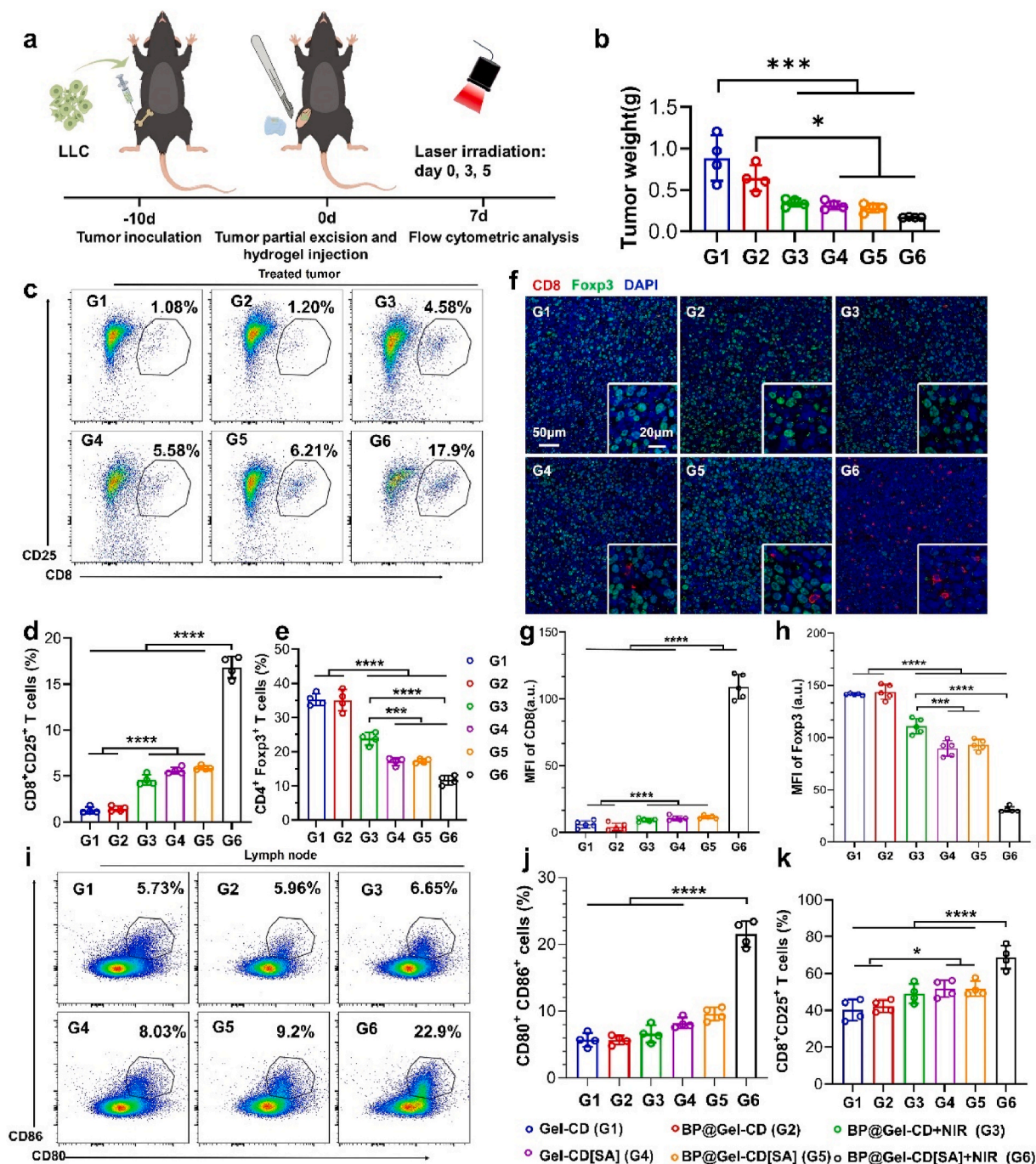


**Fig. 5.** The evaluation of hydrogels on amelioration of the immunosuppressive TME and inhibition of tumor progression. a) Timeline schematic for establishing the tumor mouse model and intervention. b) Tumor volume at the time of tissue harvesting after one week. c) Representative flow cytometry analysis of the proportion of CD8<sup>+</sup> T cells in the mouse tumor tissues from the different treatment groups. d) Quantitative percentage of CD8<sup>+</sup>CD25<sup>+</sup> T cells. e) Quantitative percentage of CD4<sup>+</sup>Foxp3<sup>+</sup> T cells. f) Representative images of multiple immunofluorescences staining for CD8 and Foxp3 in tumor tissues after one week of treatment. g-h) Average fluorescence intensity from the multiple immunofluorescence experiments for CD8 and Foxp3 in Figure f. i) Representative flow cytometry plots showing the proportion of CD80<sup>+</sup> and CD86<sup>+</sup> dendritic cells in draining lymph nodes after different treatments. j) Quantitative percentage of CD80<sup>+</sup>CD86<sup>+</sup> dendritic cells relative to CD11c<sup>+</sup> dendritic cells from Figure i. k) Quantitative percentage of CD8<sup>+</sup>CD25<sup>+</sup> T cells in draining lymph nodes after different treatments. Data are presented as mean  $\pm$  SD (n = 4–5). Statistical analysis was performed using one-way ANOVA with Tukey's post-hoc test. \*P < 0.05, \*\*P < 0.01, \*\*\*P < 0.001.

CD groups showed no complete remission, with a survival rate of only 60 % (Fig. 4c and d). As illustrated in Fig. 4e, the tumor volume in the BP@Gel-CD[SA] hydrogel + NIR group was smaller than in the other five groups. Additionally, BP@Gel-CD + NIR, Gel-CD[SA], and BP@Gel-CD[SA] exhibited inhibitory effects on tumor growth. The BP@Gel-CD[SA] + NIR treatment exhibited the best efficacy as evidenced by the highest complete remission rate and minimized tumor size.

Spleens were harvested from mice after one month for flow cytometry analysis. The proportion of CD8<sup>+</sup> T cells was significantly higher in the BP@Gel-CD[SA] + NIR group than in the other five groups (Fig. 4f), twice that in the Gel-CD and Gel-CD[SA] groups (Fig. 4g). C-C receptor 7 (CCR7) is important for T cells to migrate toward the T-cell zone of the spleen, altering memory CD8<sup>+</sup> T-cell homeostasis [21]. The BP@Gel-CD[SA] hydrogel combined with NIR irradiation demonstrated a significantly higher proportion of CD8<sup>+</sup>CCR7<sup>+</sup> T cells ( $37.93 \pm 1.24$  %) and an elevated cell count ( $6.25 \pm 0.52 \times 10^3$ ) compared to the other five experimental groups, as determined by flow cytometric analysis (Figs. S11 and S12). Similarly, quantitative analysis revealed approximately twofold increase in the proportion of mature dendritic cells in the BP@Gel-CD[SA] hydrogel combined with NIR irradiation group compared to the Gel-CD hydrogel group alone. This marked enhancement in dendritic cell maturation, as determined by surface marker expression analysis, suggests that the BP@Gel-CD[SA] hydrogel with NIR treatment may significantly promote dendritic cell maturation and subsequent antigen presentation capacity (Fig. 4h and i). The rationally designed composite hydrogel system not only achieves efficient photothermal ablation of residual tumor cells following surgical resection, but also potentiates systemic antitumor immunity through enhanced dendritic cell activation and subsequent T cell-mediated immune responses.

Moreover, all mice maintained stable body weights throughout the treatment, indicating minimal side effects of the hydrogel (Fig. S13). H&E staining of major organ tissues (liver, spleen, kidneys, heart, and lungs) showed no significant inflammation, demonstrating the favorable biosafety profile of BP@Gel-CD[SA] hydrogel + NIR treatment (Fig. S14).

## 2.5. The evaluation of hydrogels on amelioration of the immunosuppressive TME and inhibition of tumor progression

To further investigate the interaction between tumor tissue and hydrogels, we employed a femoral tumor model of C57BL/6J mice without curettage. After the tumors in these mice reached approximately 50 mm<sup>3</sup>, six groups were treated with different interventions (Gel-CD, BP@Gel-CD, BP@Gel-CD + NIR, Gel-CD[SA], BP@Gel-CD[SA], and BP@Gel-CD[SA] + NIR). Fig. 5a illustrates the tumor model and treatment regimen. After one week of interventions, the femoral graft tumors were harvested (Fig. S15). In Fig. 5b, the tumor mass in the BP@Gel-CD[SA] hydrogel + NIR group was the smallest, approximately one-fifth, and one-third of the masses in the Gel-CD and BP@Gel-CD[SA] groups, respectively. Both the BP@Gel-CD + NIR and Gel-CD[SA] groups exhibited suppression of tumor growth compared to the Gel-CD group. Then, we conducted flow cytometry analysis on the femoral graft tumors and their draining lymph nodes. The BP@Gel-CD[SA] hydrogel + NIR group exhibited the highest proportion of activated CD8<sup>+</sup> T cells (CD25<sup>+</sup>), with a percentage of  $16.84 \pm 1.18$  %, more than 10 times that of the Gel-CD ( $1.29 \pm 0.34$  %) and BP@Gel-CD ( $1.43 \pm 0.29$  %) groups. The BP@Gel-CD + NIR ( $4.57 \pm 0.55$  %) and Gel-CD[SA] ( $5.59 \pm 0.36$  %) groups also showed significantly higher proportions of CD8<sup>+</sup>CD25<sup>+</sup> T cells compared to the Gel-CD group (Fig. 5c and d). Antitumor immune responses are positively regulated by the number of functionally activated CD8<sup>+</sup> T cells and negatively regulated by regulatory T cells (Tregs), characterized by the expression of CD3, CD4, and the intracellular antigen Foxp3 [22]. Flow cytometry revealed that more than 30 % of CD4<sup>+</sup> T cells in the Gel-CD-treated tumors were Tregs (CD4<sup>+</sup>Foxp3<sup>+</sup>), while the percentage of Tregs in the BP@Gel-CD[SA] hydrogel + NIR-treated tumors significantly decreased to  $11.68 \pm$

1.34 % (Figure S16, Fig. 5e). Similarly, multiplex immunofluorescence semiquantitative data (Fig. 5f–h) indicated that the MFI of CD8 (red) was significantly increased. At the same time, the MFI of Tregs marked by Foxp3 (green) was significantly decreased after BP@Gel-CD hydrogel + NIR treatment. These data portended that the combination treatment favorably recruited CD8<sup>+</sup> T cells and reduced the proportion of Foxp3<sup>+</sup> Treg within tumors.

Furthermore, analysis of the tumor-draining lymph nodes (inguinal lymph nodes) showed that the proportion of activated DCs and activated T cells was significantly higher in the BP@Gel-CD hydrogel + NIR group compared to the other five groups (Fig. 5i, j, 5k). In conclusion, either photothermal therapy alone or SA alone can moderately enhance immune responses in tumor sites and draining lymph nodes. However, the combination of PTT and SA yielded the best results. BP@Gel-CD[SA] hydrogel + NIR can induce ICD in lung cancer bone metastases, promote DC maturation, and synergistically enhance the body's antitumor immune response by significantly increasing T lymphocyte infiltration and tumor cell killing while reducing the number of immunosuppressive Treg cells within the tumor.

To investigate the mechanism of BP@Gel-CD[SA] hydrogel + NIR treatment on the tumor microenvironment, we collected tumor tissues from the Gel-CD group and the BP@Gel-CD[SA] hydrogel + NIR group for single-cell RNA sequencing analysis (Fig. 6a).

19 distinct cell clusters were identified from harvested 38,673 cells through unsupervised clustering analysis (Fig. S17). Using cell-specific marker genes as reported, we annotated these clusters into primary cell types, including tumor cells (Myc, Rhox5) [23], immune cells (Cd3e, Cd3g, Cd3d), fibroblasts (ACTA2, COL1A1, COL1A2) [24], inflammatory cancer-associated fibroblasts (iCAFs) (PDGFRA<sup>+</sup>, CXCL12<sup>+</sup>), myofibroblast-like CAFs (ACTA2<sup>+</sup>, PDGFRA<sup>−</sup>), endothelial cells (Esm1, Pecam1, Plvap), monocytes (S100A8<sup>+</sup>S100A9<sup>+</sup>), and tumor-associated macrophages (TAMs) (APOE, CD68, Ctss, Ms4a6c) [25] (Fig. 6b and c). Following the BP@Gel-CD[SA] hydrogel + NIR treatment, the proportion of tumor cells in mouse lung cancer xenografts was reduced to 82 %, compared to 91 % in the Gel-CD group, as illustrated in Fig. 6e. Concurrently, there was a significant increase in the proportions of lymphocytes and macrophages among the non-tumor cell population (Fig. 6e). The immune cells were further categorized into CD4<sup>+</sup> T cells (CD4<sup>+</sup>CD8<sup>−</sup>), CD8<sup>+</sup> T cells (CD8a<sup>+</sup>), DCs (Irf8, Itgax), and natural killer (NK) cells (Prf1, Gzmb), as depicted in Fig. 6d and f, along with a category of undefined cells (not shown). Notably, the numbers of CD4<sup>+</sup> T cells, CD8<sup>+</sup> T cells, DCs, and NK cells increased following the BP@Gel-CD[SA] hydrogel + NIR treatment. Gene Set Enrichment Analysis (GSEA) (Fig. 6g) revealed that immune cells exhibited significantly upregulated enriched functions, including immune response, inflammatory response, and regulation of apoptotic process ( $P < 0.001$ ). This further demonstrates that the combination therapy of phototherapy and a SA can enhance the anti-tumor function of lymphocytes. Utilizing the AddmoduleScore function to evaluate the M1 and M2-like macrophage gene sets [26], we observed (Fig. 6h and i) a significant increase in the number of M1-like macrophages following the BP@Gel-CD[SA] + NIR treatment, thereby demonstrating a notable effect on anti-tumor macrophage polarization.

## 2.6. Therapeutic effects of BP@Gel-CD[SA] + NIR on distant tumors via immune activation

In patients with advanced lung cancer and bone metastases, multiple bone metastases are often present. A key clinical challenge is determining whether treating a single bone lesion can elicit an immune response that suppresses other lesions [27]. Based on the aforementioned findings demonstrating the potent immune activation of BP@Gel-CD[SA] + NIR treatment, we subsequently investigated the capacity to induce systemic antitumor immunity and therapeutic efficacy against distant tumors. We hypothesized that the hydrogel-mediated local immune activation could elicit abscopal effects through the



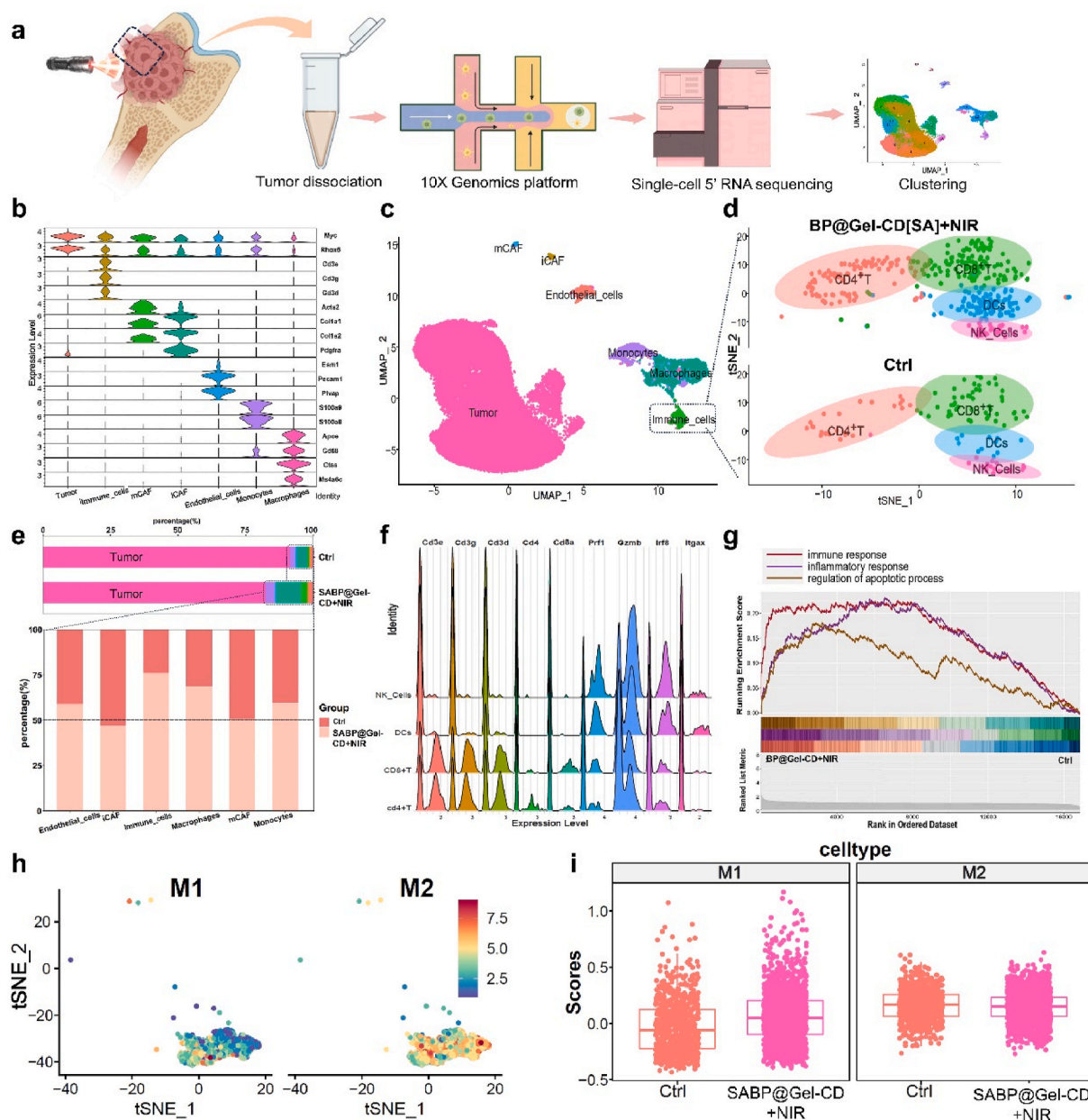


**Fig. 6.** Tumor microenvironment changes after BP@Gel-CD[SA] + NIR treatment based on Single-cell RNA sequence. **a**) Schematic diagram of Single-cell RNA sequence. **b**) Violin plot of marker genes for cell type identification. **c**) UMAP plot of cell types. **d**) The tSNE plot of immune cell subpopulations (undefined cells not shown). **e**) The proportion of cell types in tumor tissue after BP@Gel-CD[SA] + NIR treatment. **f**) Ridge plot of marker genes for immune cell identification. **g**) GSEA analysis of enriched pathways in immune cells. **h**) tSNE plots showing the expression scores of M1- and M2-like macrophage signatures in macrophages. **i**) Scores of M1 and M2-like macrophage gene sets after BP@Gel-CD[SA] + NIR treatment.

generation of tumor-specific systemic immune responses. After 3 days of injecting luciferase<sup>+</sup> LLC tumor cells into the medial femoral condyle of the mice,  $5 \times 10^5$  LLC tumor cells were injected into the contralateral femoral condyle. After 7 days, when the tumors on the treated side grew to approximately 50 mm<sup>3</sup>, 50  $\mu$ L of hydrogel from the six groups was injected into the tumor site. Laser irradiation was performed on the day of surgery, as well as on the day 3 and 5 post-surgery. On the day 7, in vivo imaging system was used to evaluate and measure the tumor size (Fig. 7a). The smallest distant tumors were observed in the BP@Gel-CD [SA] + NIR-treated group (Fig. 7b, Fig. S18); the sizes of the tumors in the photothermal therapy group (BP@Gel-CD + NIR) or the SA-treated group (Gel-CD[SA]) were not significantly different. The proportions of activated CD8<sup>+</sup> CD25<sup>+</sup> T cells and CD80<sup>+</sup> CD86<sup>+</sup> DC cells were increased considerably, reaching  $6.92 \pm 1.05$  % and  $23.45 \pm 1.7$  %,

respectively (Fig. 7c and d). Additionally, the SA-treated group (Gel-CD [SA]) also showed a twofold increase in activated DC cells compared to the Gel-CD group (Fig. 7e). Multiplex immunofluorescence semi-quantitative data from distant tumors (Fig. 7f–i) showed that the MFI of CD8 (red) was significantly increased, while the MFI of Foxp3-marked (green) Tregs was significantly decreased after BP@Gel-CD + NIR treatment. Ki67 immunofluorescence staining revealed that Ki67 expression was reduced considerably in distant tumors after BP@Gel-CD + NIR treatment while it still highly expressed in other groups (Fig. 7g). Photothermal therapy or SA treatment alone induced limited immune responses. Although high-temperature ablation can effectively eliminate the primary tumor, it has a limited effect on inhibiting distant tumors, possibly due to insufficient DC activation in the absence of immune adjuvants after thermal ablation. In summary,



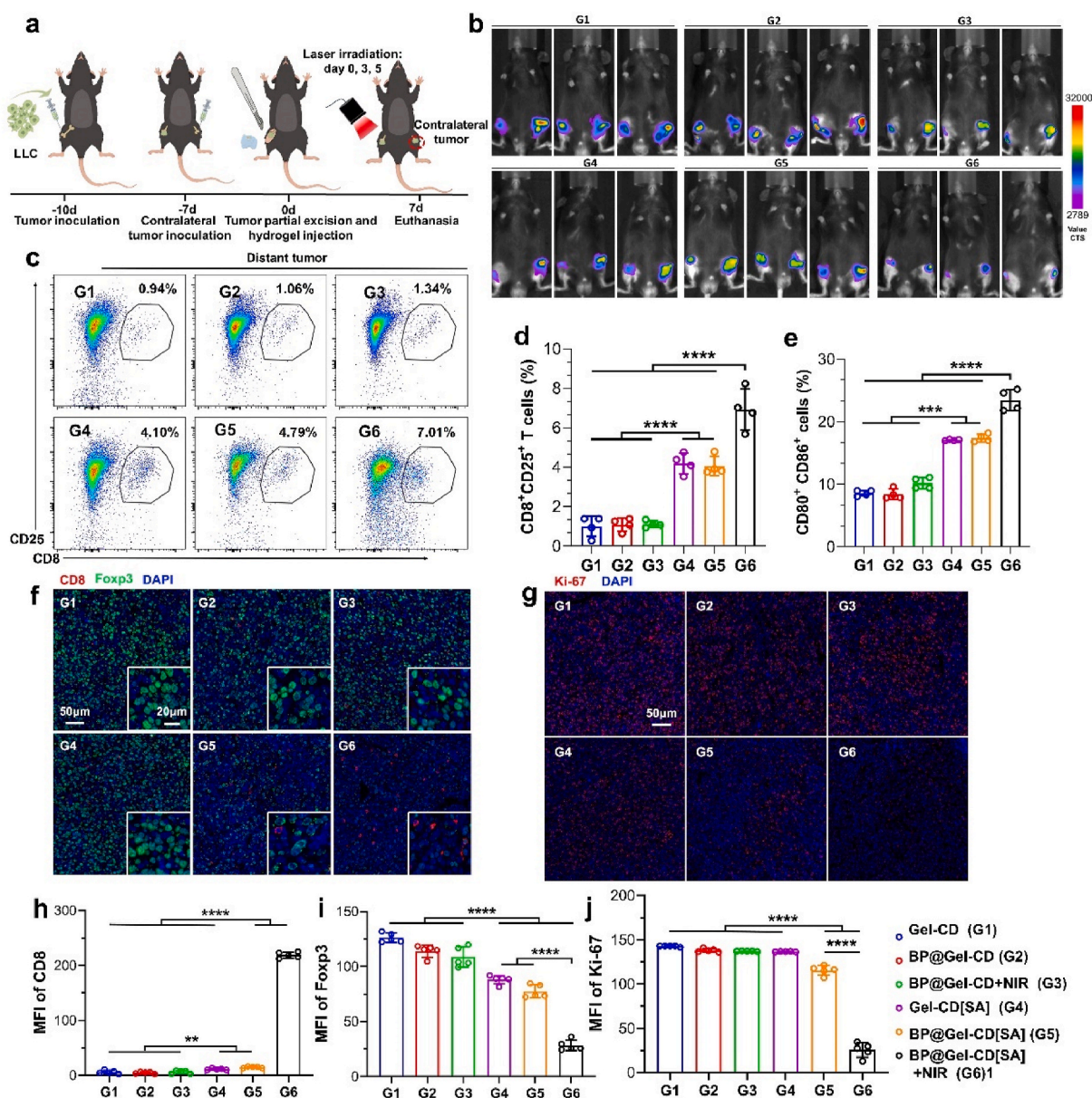


**Fig. 7.** Therapeutic Effects of BP@Gel-CD[SA] + NIR on Distant Tumors via immune activation. a) Timeline schematic for establishing the tumor mouse model and intervention. b) In vivo imaging of mice at one week. c) Representative flow cytometry plots depicting the proportion of CD8<sup>+</sup> CD25<sup>+</sup> T cells in absopal tumor tissues after different treatments. d) Quantitative percentage of CD8<sup>+</sup>CD25<sup>+</sup> T cells. e) Quantitative percentage of CD80<sup>+</sup> and CD86<sup>+</sup> in tumor-draining lymph nodes after different treatments. f) Representative images of multiple immunofluorescences staining for CD8 and Foxp3 in absopal tumor tissues one week after treatment. g) Representative images of Ki67 immunofluorescence staining in absopal tumor tissues after one week of treatment. h-j) Quantification of fluorescence intensity for CD8, Foxp3, and Ki67 in absopal tumor tissues. Data are presented as mean  $\pm$  SD (n = 4–5). Statistical analysis was performed using one-way ANOVA with Tukey's post-hoc test (GraphPad Prism 9).  $p < 0.01$ . \* $P < 0.05$ , \*\* $P < 0.01$ , \*\*\* $P < 0.001$ , and \*\*\*\* $P < 0.0001$ .

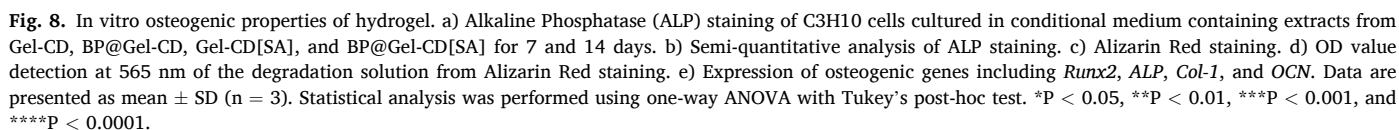
BP@Gel-CD[SA] + NIR treatment can significantly activate systemic immunity, and promote T lymphocyte infiltration and tumor cell killing, thereby inhibiting the growth of distant tumors.

## 2.7. Promotion of osteogenic function by hydrogels *In vitro* and *In vivo*

Osteolytic lesions are common in lung cancer bone metastases. After surgical curettage, bone defects remain, leading to a decrease in mechanical strength [28]. Therefore, addressing bone repair after anti-tumor therapy represents a critical and urgent challenge. BPNSs can undergo oxidative degradation in environmental conditions, primarily yielding non-toxic  $\text{PO}_4^{3-}$  as the major degradation product. This  $\text{PO}_4^{3-}$  can sequester  $\text{Ca}^{2+}$  within the body, leading to the formation of calcium phosphate deposits, which serve as a raw material for bone repair after

tumor ablation [29,30].

C3H10 cells were cultured in an osteogenic induction medium containing extract from Gel-CD, BP@Gel-CD, Gel-CD[SA], and BP@Gel-CD[SA] for 7 and 14 days, respectively, and assessed for alkaline phosphatase (ALP) activity and Alizarin Red staining. After ALP staining, cells treated with BP@Gel-CD and BP@Gel-CD[SA] extracts exhibited more intense staining (Fig. 8a, Fig. S19), indicating higher ALP activity. Further quantitative analysis of ALP activity after 14 days of culture (Fig. 8b) revealed that BP@Gel-CD and BP@Gel-CD[SA] extracts increased ALP protein expression by 2.9-fold and 2.5-fold, respectively, compared to the Gel-CD and Gel-CD[SA] groups. To confirm the effects of composite hydrogels on cell matrix mineralization, Alizarin Red staining was performed after 7 and 14 days of osteogenic induction. As shown in Fig. 8c and Fig. S20, the BP@Gel-CD and BP@Gel-CD[SA]



The expression of osteogenic-related genes was assessed using quantitative real-time PCR (Fig. 8e). After 7 days of treatment with BP@Gel-CD extract, *ALP* and *COL-1* expression increased by 7.7-fold and 2.5-fold, respectively, compared to the Gel-CD group. After 14 days, the expression of *OCN* and *COL-1* in the BP@Gel-CD[SA] group was significantly higher than in the Gel-CD[SA] group. These results

To evaluate the *in vivo* osteogenic effect of the hydrogels, a hole with a diameter of 1.5 mm was drilled through the medial femoral condyle of C57BL/6J mice. The bone defects were filled with Gel-CD, BP@Gel-CD, Gel-CD[SA], and BP@Gel-CD[SA]. At 6 weeks post-surgery, qualitative analysis using micro-CT (Fig. 9a) revealed that the trabecular bone in the Gel-CD and Gel-CD[SA] groups was relatively sparse, whereas it was denser in the BP@Gel-CD and BP@Gel-CD[SA] groups. Quantitative analysis of parameters such as BV/TV, Tb.Th, Tb.N, and BMD showed significant increases in the BP@Gel-CD group compared to the Gel-CD



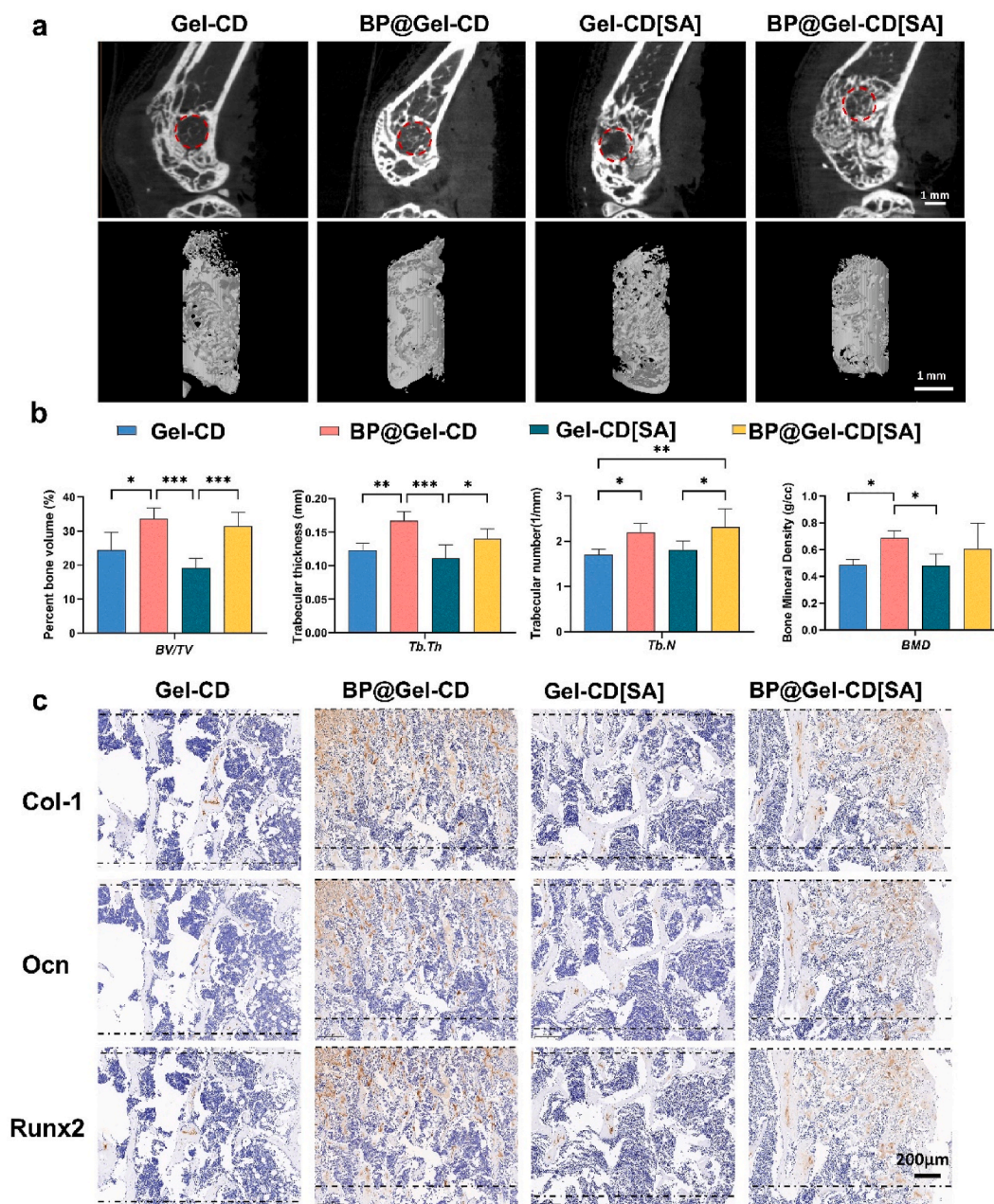


**Fig. 9.** In vivo osteogenic ability of hydrogel. a) Micro-CT images of newly formed bone at 6 weeks post-implantation in the mouse femoral condyle. scale bars = 0.75 mm. b) Quantitative analysis of BV/TV, Tb.Th, Tb.N, and BMD. c) Representative immunohistochemical staining images of newly formed bone, two parallel dashed lines indicating the bone defect region. Data are presented as mean  $\pm$  SD (n = 5). Statistical analysis was performed using one-way ANOVA with Tukey's post-hoc test. \*P < 0.05, \*\*P < 0.01, \*\*\*P < 0.001.

group (Fig. 9b). To further assess bone regeneration, HE and Masson staining of the bone defect areas was performed. HE and Masson staining showed that BP@Gel-CD and BP@Gel-CD[SA] can promote substantial new bone formation (Fig. S21). Immunohistochemical staining for COL-1, OCN, and Runx2 proteins indicated that newly formed bone tissue in the BP@Gel-CD and BP@Gel-CD[SA] groups possess higher levels of COL-1, OCN, and Runx2, indicating enhanced osteogenic activity (Fig. 9c, Fig. S22).

To demonstrate the dual therapeutic effect of SABP@Gel-CD combined with NIR, an in situ animal model was established (Fig. 4a) to evaluate its anti-tumor and bone regeneration properties. After 28 days, the bone loss was assessed using Micro-CT. The results showed that only the SABP@Gel-CD + NIR group exhibited bone regeneration, with a significant increase in both BV/TV and Tb.N compared to other

treatments (Fig. 10a–d). HE staining (Fig. 10e) confirmed that, except for the SABP@Gel-CD + NIR group, all other groups displayed more severe bone damage. In summary, SABP@Gel-CD + NIR effectively inhibits tumors and promotes bone regeneration, demonstrating practical dual therapeutic effects in the lung cancer bone metastasis model when combined with NIR-laser treatment, indicating potential for clinical translation.

### 3. Conclusion

In brief, we developed a hydrogel-based photothermal immunotherapy system utilizing SA and BPNSs. The photothermal and photodynamic activities of BPNSs can achieve hyperthermia and ROS-mediated mitochondrial damage, while also enhancing antitumor



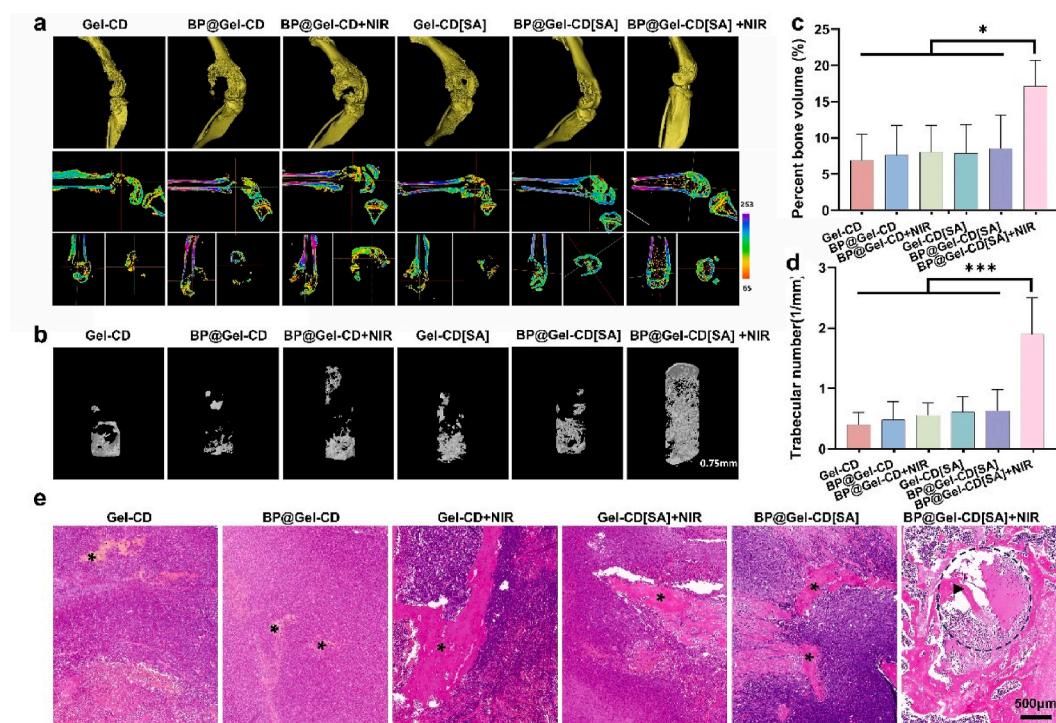


**Fig. 10.** Efficacy of the multi-faceted treatment. a) Micro-CT assessment of bone defects, the top image shows a three-dimensional reconstruction, while the bottom image displays the corresponding axial section views. b) Reconstruction of the trabecular bone in the area of the bone defect. Quantitative analysis of BV/TV (c) and Tb.N.(d) of the trabecular bone in the area of the bone defect in Fig. 10b. Data are presented as mean  $\pm$  SD ( $n = 5$ ). Statistical analysis was performed using one-way ANOVA with Tukey's post-hoc test. e) HE staining images of the defect area, \* indicates remaining bone tissue in the tumor site, the dotted circle denotes the bone defect created during operation, and ▲ indicates the trabecular bone of newly formed bone.

immunity through ICD. Local application of SA further induces the cGAS-STING pathway. Activated systemic antitumor response was achieved by combination of photothermal therapy and immunotherapy. Constructed integrative system can not only eliminate residual cells but also suppress remote tumor growth via systemic antitumor immune response in vivo. In the long term, BPNSs can promote the formation of new bone at sites of tumor-induced bone destruction, improving bone strength in the affected area. For clinical translation, our method would be particularly meaningful for late-stage multi bone metastasis of lung cancer that is not curable by conventional surgery or radiotherapy strategies.

## 4. Experimental section

### 4.1. Materials and reagents

Black phosphorus crystal powder was purchased from Nanjing XFNANO Materials Tech Co., Ltd (Nanjing, China). *N*-Methyl-2-pyrrolidone (NMP, 99.5 %, anhydrous) was obtained from Aladdin Reagents. Phenyl(2,4,6-trimethylbenzoyl)phosphinic acid lithium salt (photo-initiator, LAP) was obtained from Aladdin (Aladdin, USA). Gelatin-methacryloyl (GelMA) with 80 % of methacrylation was synthesized as described previously [31] and acrylamide-modified-cyclodextrin (AAM- $\beta$ -CD) was prepared according to a procedure in the literature [32,33]. All reagents were used as received without further purification.

Luciferase-expressing LLC(LLC-luc) cells were purchased from iCell (Shanghai, China). Fluorescein sodium salt was purchased from Macklin. SA was purchased from MedChemExpress (HY-123943).  $\beta$ -glycerol phosphate, dexamethasone, and ascorbic acid, sodium phosphatedibasic ( $\text{Na}_2\text{HPO}_4$ ), and ethylene diamine tetraacetic acid (EDTA) were bought from Sigma-Aldrich. Dulbecco's modified Eagle's medium (DMEM), Phosphate-buffered saline (PBS) were purchased from Gibco Life Sciences. Serum-free cell freezing solution (Lonsera, cat. no. LS368-001)

was purchased from Suzhou Shuangru Biotechnology. Calcein AM/PI cell viability assay kit, annexin V-FITC apoptosis detection kit, and DCFH-DA were also acquired from Meilun Biotechnology Co. (Dalian, China).

The following antibodies were applied for flow cytometry: anti-mouse CD11c (clone N418, Biolegend, 1:200 diluted), anti-mouse MHC II (clone M5/114.15.2, Biolegend, 1:200 diluted), anti-mouse CD80 (clone 16-10A1, Biolegend, 1:200 diluted), anti-mouse CD86 (clone GL1, Biolegend, 1:200 diluted), anti-mouse CD45 (clone 30-F11, BD Biosciences, 1:200 diluted), anti-mouse CD3 (clone 17A2, Biolegend, 1:400 diluted), anti-mouse CD4 (clone GK1.5, BD Biosciences, 1:200 diluted), anti-mouse CD8 (clone 53-6.7, Biolegend, 1:200 diluted), anti-mouse CD25 (clone PC61, Biolegend, 1:200 diluted), anti-mouse Foxp3 (clone FJK-16s, Thermo Fisher, 1:100 diluted). FVS 780 (Fixable Viability Dye eFlour™ 780, eBioscience, 65-0865-14, USA, 1:100 diluted) was used for live or dead cells selection. The anti-STING antibody (ab288157), anti-NAK/TBK1 antibody (ab40676), anti-IRF3 antibody (ab68481) were purchased from Abcam. The phospho-IRF3 (Ser396) antibody (AF2436), phospho-TBK1 (Ser172) antibody (AF8190) and phospho-TMEMM173/STING (Ser366) antibody (AF7416) were purchased from Affinity Biosciences. RIPA lysate, protease phosphatase inhibitor, ultra-sensitive ECL chemiluminescence kit were obtained from Beyotime (Shanghai, China).

Lewis lung carcinoma (LLC) cells and NSCLC cells A549 were cultured in Dulbecco's Modified Eagle Medium (DMEM) containing 10 % fetal bovine serum (FBS), at 37 °C, 5 %  $\text{CO}_2$ . BMDCs were extracted from 6-week-old C57BL/6J mice and maintained via a standard method used in previous studies [34]. C3H/10T1/2 (C3H10) cells were cultured in  $\alpha$ -MEM medium supplemented with 10 % FBS.

### 4.2. Preparation and characterization of BP@Gel-CD hydrogel

Liquid phase exfoliation method was used to prepare the black

phosphorus nanosheets (BPNSs) [35,36]. First, the black phosphorus crystal powder was dispersed in ultrapure water. The mixture was sonicated for 9 h in an ice bath using a cell disruptor to obtain a brown dispersion. After that, the dispersion was sonicated in an ice bath for 4 h, and the supernatant was collected after centrifugation (10000 rpm) for 20 min. To further obtain the hydrogel, the pregel solution was first prepared by dissolving 10 w/v% GelMA, 4w/v% AAm- $\beta$ -CD, and 0.5w/v% photoinitiator (LAP) in DPBS. After that, BPNSs were dispersed in the pregel solution at a final concentration of 200 ppm and further polymerized by UV irradiation (405 nm, 60 s) to produce the BP@Gel-CD hydrogel.

The morphology of the hydrogels coated with platinum was observed by using field-emission scanning electron microscopy (SEM, MERLIN, Zeiss, Germany) at an acceleration voltage ranging from 5 to 10 kV. Strain sweep testing was conducted by Rheometer (MCR 302, Anton Paar) to analyze the storage modulus ( $G'$ ) and loss modulus ( $G''$ ) of hydrogels in the range of 0.01–2000 % shearing strain. Dynamic mechanical testing (DMA Q800, TA Instruments, USA) was also applied to evaluate the mechanical properties of the hydrogels. The hydrogels were prepared into a cylindrical shape with a diameter of  $\approx 10$  mm and a thickness of  $\approx 5$  mm. In the static compression mode, the compression test was performed at a strain rate of  $10\% \text{ min}^{-1}$ . The in vitro photo-thermal properties of the hydrogels were investigated by NIR irradiation of the hydrogels at a power density of  $1 \text{ W/cm}^2$  with an 808 nm laser. The temperature values of the irradiated sites and the corresponding thermal images were recorded on an infrared thermal imager (FLIRTM A325SC camera, USA).

#### 4.3. Synthesis and characterization of the SA encapsulated BP@Gel-CD hydrogel

AAM-CD loaded with STING (AAM- $\beta$ -CD[SA]) was prepared by mixing SA (50 mg) and AAM- $\beta$ -CD (160 mg) in ultrapure water and stirring for 24 h in the dark. During this process, hydrophobic interactions inserted STING into the hydrophobic cavity of AAM- $\beta$ -CD in the aqueous solution. After that, AAM- $\beta$ -CD[SA] was obtained by lyophilization for 72 h at  $-80^\circ\text{C}$  and characterized by NMR spectroscopy (400 MHz, Bruker, Germany). Then, the pre-gel solution was prepared by dissolving 10w/v% GelMA, 4w/v% AAM- $\beta$ -CD[SA], and 0.5w/v% photoinitiator (LAP) in DPBS, and BPNSs were added to the pregel solution, at a final concentration of 200 ppm. SA-encapsulated BP@Gel-CD nanocomposite hydrogel (BP@Gel-CD[SA]) was further formed through the photocrosslinking of the pre-gel solution initiated by UV treatment (405 nm) for 1 min at  $25^\circ\text{C}$ .

The freeze-dried BP@Gel-CD[SA] hydrogel was characterized by Fourier infrared spectrophotometer (FTIR, CCR-1, Thermo Scientific, USA). The concentration of SA released from the inside of the hydrogel was determined by high-performance liquid chromatography (HPLC, AB Sciex, USA). Briefly, 300  $\mu\text{L}$  hydrogel were soaked in PBS (600  $\mu\text{L}$ ) at the condition of  $37^\circ\text{C}$  and 100 rpm. Release medium was collected at the set time points and the amount of the released SA was measured by HPLC. The release percentage of SA was calculated based on the total amount of SA encapsulated in the BP@Gel-CD hydrogel. A standard curve of SA in the range of 0.01–0.5  $\mu\text{g/mL}$  was used to quantify the amount of SA released.

#### 4.4. Cytotoxicity assay and ROS detection

A549 cells were first seeded in a 24-well plate at a density of  $3 \times 10^4$  cells per well overnight and then incubated with different treatments as follows: 1) Gel-CD; 2) BP@Gel-CD; 3) Gel-CD + NIR; 4) BP@Gel-CD + NIR. The two NIR groups were followed by 803-nm laser irradiation at a power intensity of  $0.5 \text{ W/cm}^2$  for 0, 2.5min, 5 min, 10min, respectively. After another 2 h incubation, the cell viabilities of these treated cells were stained by calcein-AM and propidium iodide (PI) (Beyotime, China) under a standard protocol. After washing with PBS, cells were

stained with Calcein-AM (1X) and PI dyes (1X) for 15 min and examined using a fluorescence microscope. Also, after those treatment, cell apoptosis was analyzed using the flow cytometry with an Annexin V-FITC/PI Apoptosis Detection kit (Solarbio, China). ROS generation was determined using a ROS Assay Kit (Beyotime, China). The cells were stained with 10  $\mu\text{M}$  DCFH-DA at  $37^\circ\text{C}$  for 20 min in the dark and then incubated with: 1) Gel-CD; 2) BP@Gel-CD; 3) Gel-CD + NIR; 4) BP@Gel-CD + NIR. Then the cells were imaged using a fluorescence microscope.

#### 4.5. DC maturation in vitro

LLC cells were inoculated in a 6-well tissue culture plate at a density of  $3 \times 10^5$  cells per well and incubated with Gel-CD, BP@Gel-CD, BP@Gel-CD + NIR, Gel-CD[SA], BP@Gel-CD[SA] and BP@Gel-CD[SA]+NIR for 24 h. BMDC cells were then co-cultured with pretreated LLC cells for another 24 h. The cells were stained with anti-CD80-APC and anti-CD86-FITC to analyze DC maturation by flow cytometry assay.

#### 4.6. Detection of osteogenic mRNA expression

For osteogenic induction, the medium of C3H10 was replaced with an osteogenic induction medium (containing 50  $\mu\text{M}$  ascorbic acid, 10 mM  $\beta$ -glycerophosphate, and 100 nM dexamethasone) and extracts from Gel-CD, BP@Gel-CD, Gel-CD[SA], and BP@Gel-CD[SA] every 3 days. The cells were subjected to RT-PCR to detect mRNA expression of osteogenic genes including Runx-2, ALP, Collagen-1, and OCN. Briefly, total RNA was isolated from C3H10 cells using the E.Z.N.A.® Total RNA Kit I (OMEGA, USA). Afterward, RT-PCR was carried out using the TransScript® II Green One-Step qRT-PCR SuperMix (TransGen Biotech, China). Primer sequences of Runx-2, ALP, Collagen-1, and OCN are shown in Table S1. The relative mRNA expression was calculated using the comparative cycle threshold (CT) method ( $\Delta\Delta\text{CT}$  method), and all the experiments were performed in triplicate.

#### 4.7. Alizarin red and alkaline phosphatase (ALP) staining

Alizarin red and ALP staining were performed to detect the extracellular matrix mineralization. After osteogenic induction in each extract for 7 and 14 d, the C3H10 cells were fixed and stained with Alizarin Red S solution (ARS, Sigma, USA) to detect calcium deposition. The differentiation ability of the cells was quantitatively evaluated by eluting the stained wells with a solution of 10 % cetylpyridinium chloride (Sigma, USA) and the optical density were measured at 620 nm. The ALP activity was quantified by p-nitrophenyl phosphate (pNPP) (Sigma, StLouis, MO, USA) according to the described procedures. Briefly, total protein was extracted by RIPA (Beyotime, China), and the protein content was determined by the bicinchoninic acid (BCA) Protein Assay Kit (Beyotime, China). The results were normalized to the total intracellular protein content and expressed in nanomoles of produced p-nitrophenol per min per mg of protein (nmol/min/mg protein). Furthermore, ALP expression was visualized by BCIP-NBT staining (Beyotime, China) method.

#### 4.8. Evaluation of STING activation

To examine the in vitro activation of STING induced by BP@Gel-CD [SA], a Western blot analysis was conducted to assess the expression levels of phosphorylated TBK1 (p-TBK1) and phosphorylated IRF3 (p-IRF3) across multiple experimental groups. LLC cells were plated in 6-well tissue culture plates at a density of  $3 \times 10^5$  cells per well and subjected to various treatments including Gel-CD, BP@Gel-CD, BP@Gel-CD + NIR irradiation, Gel-CD[SA], BP@Gel-CD[SA], and BP@Gel-CD [SA] + NIR irradiation. Subsequently, the cells were lysed using RIPA lysis buffer supplemented with 1 % protease inhibitor and phosphatase inhibitors. The total protein concentration was determined utilizing the BCA Protein Assay Kit (cat. no. 23209, Thermo Scientific). Equal protein

aliquots were mixed with an equivalent volume of  $4 \times$  loading buffer and heated to  $100^\circ\text{C}$  for 15 min. SDS-PAGE then resolved the proteins with 10 % polyacrylamide gels (PG212, EpiZyme). The resolved proteins were transferred to a PVDF membrane at a constant current of 400 mA for 60 min. Following the transfer, the membrane was blocked with 2 % BSA in TBST for 1 h at room temperature. Subsequently, the membrane was incubated with the primary antibody overnight at  $4^\circ\text{C}$ . After five washes with TBST, the membrane was incubated with HRP-conjugated goat-developed anti-rabbit (Abcam, ab6721) secondary antibodies for 1 h at room temperature, followed by an additional 3 washes with TBST. Western blot membranes were developed with ECL, and signals were detected with ChemiDoc XRS+ (Bio-Rad) as per the manufacturer's instruction. The bands were meticulously inspected, and the expression levels of the target proteins were semi-quantified using ImageJ software (NIH, USA).

#### 4.9. *In vivo* antitumor model

The Ethics Committee of Guangdong Provincial People's Hospital approved animal experiment protocols (KY-D-2021.272) and all the animals were purchased from Guangdong Medical Laboratory Animal Center. A mouse model of femoral-transplanted tumor was established. Five-week-old male C57BL/6J mice were acclimated for one week before being injected with a suspension of LLC-luc cells in PBS (pH = 7.4) (100  $\mu\text{L}$  containing  $5 \times 10^5$  cells) into the distal metaphysis of the left femur of each mouse. When the tumor volume reached  $50\text{ mm}^3$ , the mice were randomly divided into six groups of five animals each. The tumors were then palliatively resected, and the tumor-bearing mice in each group were subjected to the following interventions: 50  $\mu\text{L}$  of Gel-CD, BP@Gel-CD, BP@Gel-CD + NIR, Gel-CD[SA], BP@Gel-CD[SA], and BP@Gel-CD[SA] + NIR. The total amount of SA was 10  $\mu\text{g}$  per mice. Laser irradiation (1 W/ $\text{cm}^2$ , 5 min) was applied on the day of surgery, as well as on the third and fifth days. The maximum temperature at the tumor site during NIR treatment was continuously monitored and precisely maintained around  $50^\circ\text{C}$  (Fig. 4b). Real-time thermal imaging (FLIR A315, USA) was utilized to ensure strict control over the local temperature during irradiation, and the exposure time was adjusted accordingly to prevent overheating.

Tumor volume was measured every three days using formula  $V = (\text{width})^2 \times \text{length} / 2$ . At 10, 18, and 28 days, the mice were anesthetized with isoflurane gas and injected intraperitoneally with fluorescein sodium substrate. *In vivo* imaging analysis was then performed using the Luznoche® Animal Imaging System (SpectralMagic, USA) and Lab-Magic software. After two weeks, spleens were harvested from the mice for flow cytometry analysis. Then, spleen samples were crushed using a rubber-headed pestle, filtered through a 200-mesh sieve to remove fat and fascia, and centrifuged at  $4^\circ\text{C}$  (400XG, 5 min). The cells were resuspended in PBS, incubated with fluorescently labeled antibodies for 40 min, and then analyzed by flow cytometry to determine the proportion of target cells (activated DCs, T cells). Tumor tissues were fixed in 10 % paraformaldehyde and processed into H&E stained sections, as well as CD8 and Foxp3 immunofluorescent stained sections.

#### 4.10. Single-cell RNA-sequencing procedure

The procured and washed tissue micro-fragments were subjected to a dissociation solution consisting of 0.35 % collagenase IV, 2 mg/ml papain, and 120 Units/ml DNase. Subsequently, the dissociation process was terminated by  $1 \times$  PBS containing 10 % FBS. Erythrocytes were removed using 1 ml of  $1 \times$  erythrocyte lysis buffer (MACS 130-094-183). Dead cells were eliminated using Dead Cell Removal MicroBeads (MACS 130-090-101). Cell viability was assessed via trypan blue staining, with a requirement of  $>85\%$  viability and a cell concentration ranging from 700 to 1200 cells/ $\mu\text{L}$ .

The single-cell suspension was then loaded onto a 10x Genomics Chromium Next GEM Single Cell 5' Kit (v2) chip as per the

manufacturer's instructions, targeting the capture of 8000 single cells. cDNA amplification and library preparation were conducted according to the standard protocol. LC-Bio Technology (Hangzhou, China) performed sequencing of the libraries on the Illumina NovaSeq 6000 sequencing system (paired-end sequencing, 150 bp), with a sequencing depth of at least 20,000 reads per cell.

The raw sequencing data from the Illumina platform were converted into FASTQ format using the bcl2fastq software (version 5.0.1). The scRNA-seq sequencing data were aligned to the reference genome, and cellular and individual 5' end transcripts were identified and counted within the sequenced samples using Cell Ranger software. The Cell Ranger output data were loaded into Seurat (version 4.1.0) to filter low-quality cells, reduce dimensionality, and cluster the scRNA-seq data. The threshold for filtering low-quality cells was set at  $>500$  genes expressed per cell and  $<25\%$  of mitochondrial gene expression within each cell. t-SNE or UMAP was utilized to project the cells into a 2D space.

Cell types were annotated using previously reported cell-specific marker genes and top-ranked differentially expressed genes. Differential genes obtained for each cell type underwent enrichment analysis based on GO (Gene Ontology, <http://geneontology.org/>) and KEGG (Kyoto Encyclopedia of Genes and Genomes) databases [37]. Significance levels of pathways were calculated using the Fisher's exact test, and gene enrichment results relevant to the cell types were selected. GSEA was performed using GSEA software (<http://www.broadinstitute.org/gsea/>).

#### 4.11. Mouse model of femoral bone defect

The mouse model of metaphyseal defect of the femur was established as previously described [38]. A 10-mm incision was made on the lateral side of the femur of C57BL/6J mice, and a 1.5-mm drill bit was used to penetrate the lateral cortical bone into the metaphyseal cancellous bone, creating a defect in the supracondylar region of the right femur. Then, hydrogels were injected into the defect site. At six weeks, the femurs were harvested. The  $\mu\text{CT}$  imaging system ( $\mu\text{CT}50$ , Scanco Medical, Brüttisellen, Switzerland) was employed to evaluate osteogenesis within the defect region. The specimens were scanned with the following parameters: voltage, 70 kV; electric current, 114  $\mu\text{A}$ ; and resolution of 10  $\mu\text{m}$  per pixel. Following scanning, a three-dimensional (3D) image was reconstructed. Bone mineral density (BMD), bone volume/total tissue volume (BV/TV), trabecular number (Tb.N), and trabecular thickness (Tb.Th) in the bone defect were analyzed using software (Scanco Medical AG, Switzerland).

After  $\mu\text{CT}$  scanning, the samples were decalcified in 10 % EDTA (pH = 7.4) and then embedded in paraffin. For microstructure observation, four longitudinal sections (150  $\mu\text{m}$  thick) of each specimen were prepared for hematoxylin and eosin (H&E), Masson-trichrome, and immunohistochemical (IHC) stainings. IHC staining was accomplished using antibodies RUNX-2 (RM8028, Biodragon).

#### 4.12. Statistical analysis

All data are presented as the mean  $\pm$  standard deviation (SD). Student's t-test evaluated differences between the experimental and control groups. One-way analysis of variance (ANOVA) was used for multiple comparisons in this study. A P value  $< 0.05$  was considered statistically significant. \*P  $< 0.05$ , \*\*P  $< 0.01$ , \*\*\*P  $< 0.001$ , and \*\*\*\*P  $< 0.0001$ . All data analysis was conducted using SPSS 22.0 analysis software (SPSS Inc, Chicago, IL).

#### CRediT authorship contribution statement

**Guoqing Zhong:** Writing – original draft, Methodology, Investigation. **Yali Miao:** Supervision, Methodology, Investigation, Data curation. **Jielong Zhou:** Writing – original draft, Methodology, Investigation, Conceptualization. **Yijie He:** Resources, Formal analysis.



**Wenjie Yang:** Writing – review & editing, Project administration, Formal analysis. **Chongquan Huang:** Writing – review & editing, Investigation. **Yunhui Zhang:** Writing – review & editing, Software, Formal analysis. **Jin Xiao:** Writing – review & editing, Funding acquisition. **Bingqing Bai:** Validation, Methodology, Data curation. **Jiaqi Zhou:** Writing – review & editing, Project administration, Methodology, Data curation. **Renshan Li:** Visualization, Methodology. **Tiantian Wei:** Project administration, Investigation, Conceptualization. **Yu Zhang:** Writing – review & editing, Project administration, Funding acquisition, Conceptualization. **Shi Cheng:** Writing – review & editing, Funding acquisition, Conceptualization.

## Data availability statement

The data supporting this study's findings are available from the corresponding author upon reasonable request.

## Ethics approval and consent to participate

The Ethics Committee of Guangdong Provincial People's Hospital approved animal experiment protocols (KY-D-2021.272) and all the animals were purchased from Guangdong Medical Laboratory Animal Center.

## Declaration of competing interest

The authors declare that they have no known competing financial interests or personal relationships that could have appeared to influence the work reported in this paper.

## Acknowledgments

The authors gratefully acknowledge the support from the National Natural Science Foundation of China (32201103, U21A2084), NSFC Incubation Project of Guangdong Provincial People's Hospital (No. KY0120220044), Guangdong Province Chinese Medicine Bureau project (20241004), Young Science and Technology Talent Support Program of Guangdong Precision Medicine Application Association (YSTTGDP-MAA202502) and the Guangdong Basic and Applied Basic Research Foundation (2022A1515110882). We thank for the website of Home for Researchers, Figdraw and Biorender support for drawing the illustration.

## Appendix A. Supplementary data

Supplementary data to this article can be found online at <https://doi.org/10.1016/j.bioactmat.2025.06.008>.

## References

- [1] A. Leiter, R.R. Veluswamy, J.P. Wisnivesky, The global burden of lung cancer: current status and future trends, *Nat. Rev. Clin. Oncol.* 20 (2023) 624–639, <https://doi.org/10.1038/s41571-023-00798-3>.
- [2] L.C. Hofbauer, A. Bozec, M. Rauner, F. Jakob, S. Perner, K. Pantel, Novel approaches to target the microenvironment of bone metastasis, *Nat. Rev. Clin. Oncol.* 18 (2021) 488–505, <https://doi.org/10.1038/s41571-021-00499-9>.
- [3] A.G. Abbott, D.E. Meyers, G. Elmi-Assadzadeh, I. Stukalin, A. Marro, S.K.T. Puloski, D.G. Morris, W.Y. Cheung, M.J. Monument, Effectiveness of immune checkpoint inhibitor therapy on bone metastases in non-small-cell lung cancer, *Front. Immunol.* 15 (2024) 1379056, <https://doi.org/10.3389/fimmu.2024.1379056>.
- [4] Y.-J. Zhu, X.-S. Chang, R. Zhou, Y.-D. Chen, H.-C. Ma, Z.-Z. Xiao, X. Qu, Y.-H. Liu, L.-R. Liu, Y. Li, Y.-Y. Yu, H.-B. Zhang, Bone metastasis attenuates efficacy of immune checkpoint inhibitors and displays “cold” immune characteristics in Non-small cell lung cancer, *Lung Cancer Amst, Neth* 166 (2022) 189–196, <https://doi.org/10.1016/j.lungcan.2022.03.006>.
- [5] Y. Wan, L.-H. Fu, C. Li, J. Lin, P. Huang, Conquering the hypoxia limitation for photodynamic therapy, *Adv. Mater. Deerfield Beach Fla* 33 (2021) e2103978, <https://doi.org/10.1002/adma.202103978>.
- [6] Y. Liu, X. Zhu, Z. Wei, W. Feng, L. Li, M. Ma, F. Li, J. Zhou, Customized photothermal therapy of subcutaneous orthotopic cancer by multichannel luminescent nanocomposites, *Adv. Mater. Deerfield Beach Fla* 33 (2021) e2008615, <https://doi.org/10.1002/adma.202008615>.
- [7] Y. Xiong, Y. Rao, J. Hu, Z. Luo, C. Chen, Nanoparticle-based photothermal therapy for breast cancer noninvasive treatment, *Adv. Mater. Deerfield Beach Fla* (2023) e2305140, <https://doi.org/10.1002/adma.202305140>.
- [8] X. Liu, M. Shen, T. Bing, X. Zhang, Y. Li, Q. Cai, X. Yang, Y. Yu, A bioactive injectable hydrogel regulates tumor metastasis and wound healing for melanoma via NIR-light triggered hyperthermia, *Adv. Sci.* (2024) 2402208, <https://doi.org/10.1002/advsc.202402208>.
- [9] Z. Sun, H. Xie, S. Tang, X.-F. Yu, Z. Guo, J. Shao, H. Zhang, H. Huang, H. Wang, P. K. Chu, Ultrasmall black phosphorus quantum dots: synthesis and use as photothermal agents, *Angew. Chem. Int. Ed Engl.* 54 (2015) 11526–11530, <https://doi.org/10.1002/anie.201506154>.
- [10] Y. Wu, Q. Liao, L. Wu, Y. Luo, W. Zhang, M. Guan, H. Pan, L. Tong, P.K. Chu, H. Wang, ZnL2-BPs integrated bone scaffold under sequential photothermal mediation: a win-win strategy delivering antibacterial therapy and fostering osteogenesis thereafter, *ACS Nano* 15 (2021) 17854–17869, <https://doi.org/10.1021/acsnano.1c06062>.
- [11] J. Zheng, J. Mo, T. Zhu, W. Zhuo, Y. Yi, S. Hu, J. Yin, W. Zhang, H. Zhou, Z. Liu, Comprehensive elaboration of the cGAS-STING signaling axis in cancer development and immunotherapy, *Mol. Cancer* 19 (2020) 133, <https://doi.org/10.1186/s12943-020-01250-1>.
- [12] B.-S. Pan, S.A. Perera, J.A. Piesvaux, J.P. Presland, G.K. Schroeder, J.N. Cumming, B.W. Trotter, M.D. Altman, A.V. Buevich, B. Cash, S. Cemerski, W. Chang, Y. Chen, P.J. Dandliker, G. Feng, A. Haidle, T. Henderson, J. Jewell, I. Kariv, I. Knemeyer, J. Kopinja, B.M. Lacey, J. Laskey, C.A. Lesburg, R. Liang, B.J. Long, M. Lu, Y. Ma, E. C. Minnihan, G. O'Donnell, R. Otte, L. Price, L. Rakhilina, B. Sauvagnat, S. Sharma, S. Tyagarajan, H. Woo, D.F. Wyss, S. Xu, D.J. Bennett, G.H. Addona, An orally available non-nucleotide STING agonist with antitumor activity, *Science* 369 (2020) eaba6098, <https://doi.org/10.1126/science.aba6098>.
- [13] E.L. Dane, A. Belessiotis-Richards, C. Backlund, J. Wang, K. Hidaka, L.E. Milling, S. Bhagchandani, M.B. Melo, S. Wu, N. Li, N. Donahue, K. Ni, L. Ma, M. Okaniwa, M.M. Stevens, A. Alexander-Katz, D.J. Irvine, STING agonist delivery by tumour-penetrating PEG-lipid nanodiscs primes robust anticancer immunity, *Nat. Mater.* 21 (2022) 710–720, <https://doi.org/10.1038/s41563-022-01251-z>.
- [14] X. Zhang, J. Tang, C. Li, Y. Lu, L. Cheng, J. Liu, A targeting black phosphorus nanoparticle based immune cells nano-regulator for photodynamic/photothermal and photo-immunotherapy, *Bioact. Mater.* 6 (2021) 472–489, <https://doi.org/10.1016/j.bioactmat.2020.08.024>.
- [15] Y. Ma, Y. Zhang, X. Li, Y. Zhao, M. Li, W. Jiang, X. Tang, J. Dou, L. Lu, F. Wang, Y. Wang, Near-infrared II phototherapy induces deep tissue immunogenic cell death and potentiates cancer immunotherapy, *ACS Nano* 13 (2019) 11967–11980, <https://doi.org/10.1021/acsnano.9b06040>.
- [16] W. Ma, R. Sun, L. Tang, Z. Li, L. Lin, Z. Mai, G. Chen, Z. Yu, Bioactivable STING nanoagonists to synergize NIR-II mild photothermal therapy primed robust and long-term anticancer immunity, *Adv. Mater.* 35 (2023) 2303149, <https://doi.org/10.1002/adma.202303149>.
- [17] M. Wang, X. Zhang, B. Liu, C. Liu, C. Song, Y. Chen, Y. Jin, J. Lin, P. Huang, S. Xing, Immunotherapeutic hydrogel with photothermal induced immunogenic cell death and STING activation for post-surgical treatment, *Adv. Funct. Mater.* 33 (2023) 2300199, <https://doi.org/10.1002/afm.202300199>.
- [18] L. Z. W. D. Z. J. X. P. Z. Z. X. W. S. L. cGAS-STING signaling in the tumor microenvironment, *Cancer Lett.* 577 (2023), <https://doi.org/10.1016/j.canlet.2023.216409>.
- [19] Y. Zhang, S. Ma, X. Liu, Y. Xu, J. Zhao, X. Si, H. Li, Z. Huang, Z. Wang, Z. Tang, W. Song, X. Chen, Supramolecular assembled programmable nanomedicine as in situ cancer vaccine for cancer immunotherapy, *Adv. Mater.* 33 (2021) 2007293, <https://doi.org/10.1002/adma.202007293>.
- [20] G. Zhong, L. Zeng, Y. He, X. Zeng, W. Huang, T. Yang, X. Chu, J. Xiao, D. Yin, Y. Chang, S. Cheng, Y. Zhang, The effects of combined microwave ablation and open surgery for the treatment of lung cancer-derived thoracolumbar metastases, *Orthop. Surg.* 14 (2022) 1300–1308, <https://doi.org/10.1111/os.13236>.
- [21] Y.W. Jung, H.G. Kim, C.J. Perry, S.M. Kaech, CCR7 expression alters memory CD8 T-cell homeostasis by regulating occupancy in IL-7- and IL-15-dependent niches, *Proc. Natl. Acad. Sci. U. S. A.* 113 (2016) 8278–8283, <https://doi.org/10.1073/pnas.1602899113>.
- [22] K. Taylor, H. Loo Yau, A. Chakravarthy, B. Wang, S.Y. Shen, I. Ettayebi, C.A. Ishak, P.L. Bedard, A. Abdul Razak, A. R Hansen, A. Spreafico, D. Cescon, M.O. Butler, A. M. Oza, S. Lheureux, N. Stjepanovic, B. Van As, S. Boross-Harmer, L. Wang, T. J. Pugh, P.S. Ohashi, L.L. Siu, D.D. De Carvalho, An open-label, phase II multicohort study of an oral hypomethylating agent CC-486 and durvalumab in advanced solid tumors, *J. Immunother. Cancer* 8 (2020) e000883, <https://doi.org/10.1136/jitc-2020-000883>.
- [23] H. Yang, Z. Lei, J. He, L. Zhang, T. Lai, L. Zhou, N. Wang, Z. Tang, J. Sui, Y. Wu, Single-cell RNA sequencing reveals recruitment of the M2-like CCL8high macrophages in Lewis lung carcinoma-bearing mice following hypofractionated radiotherapy, *J. Transl. Med.* 22 (2024) 306, <https://doi.org/10.1186/s12967-024-05118-6>.
- [24] J. Hu, Z. Chen, L. Bao, L. Zhou, Y. Hou, L. Liu, M. Xiong, Y. Zhang, B. Wang, Z. Tao, K. Chen, Single-cell transcriptome analysis reveals intratumoral heterogeneity in ccRCC, which results in different clinical outcomes, *Mol. Ther. J. Am. Soc. Gene Ther.* 28 (2020) 1658–1672, <https://doi.org/10.1016/j.jymthe.2020.04.023>.
- [25] W. Liu, H. Hu, Z. Shao, X. Lv, Z. Zhang, X. Deng, Q. Song, Y. Han, T. Guo, L. Xiong, B. Wang, Y. Zhang, Characterizing the tumor microenvironment at the single-cell level reveals a novel immune evasion mechanism in osteosarcoma, *Bone Res* 11 (2023) 4, <https://doi.org/10.1038/s41413-022-00237-6>.

- [26] E. Azizi, A.J. Carr, G. Plitas, A.E. Cornish, C. Konopacki, S. Prabhakaran, J. Nainys, K. Wu, V. Kiseliovas, M. Setty, K. Choi, R.M. Fromme, P. Dao, P.T. McKenney, R. C. Wasti, K. Kadaveru, L. Mazutis, A.Y. Rudensky, D. Pe'er, Single-cell map of diverse immune phenotypes in the breast tumor microenvironment, *Cell* 174 (2018) 1293–1308.e36, <https://doi.org/10.1016/j.cell.2018.05.060>.
- [27] X. Li, S. Khorsandi, Y. Wang, J. Santelli, K. Huntoon, N. Nguyen, M. Yang, D. Lee, Y. Lu, R. Gao, B.Y.S. Kim, C. de Gracia Lux, R.F. Mattrey, W. Jiang, J. Lux, Cancer immunotherapy based on image-guided STING activation by nucleotide nanocomplex-decorated ultrasound microbubbles, *Nat. Nanotechnol.* 17 (2022) 891–899, <https://doi.org/10.1038/s41565-022-01134-z>.
- [28] D.R. Fourney, E.M. Frangou, T.C. Ryken, C.P. Dipaola, C.I. Shaffrey, S.H. Berven, M.H. Bilsky, J.S. Harrop, M.G. Fehlings, S. Boriani, D. Chou, M.H. Schmidt, D. W. Polly, R. Biagini, S. Burch, M.B. Dekutoski, A. Ganju, P.C. Gerszten, Z. L. Gokaslan, M.W. Groff, N.J. Liebsch, E. Mendel, S.H. Okuno, S. Patel, L.D. Rhines, P.S. Rose, D.M. Sciubba, N. Sundaresan, K. Tomita, P.P. Varga, L.R. Vialle, F. D. Vrionis, Y. Yamada, C.G. Fisher, Spinal instability neoplastic score: an analysis of reliability and validity from the spine oncology study group, *J. Clin. Oncol. Off. J. Am. Soc. Clin. Oncol.* 29 (2011) 3072–3077, <https://doi.org/10.1200/JCO.2010.34.3897>.
- [29] M. Goretti Penido, U.S. Alon, Phosphate homeostasis and its role in bone health, *Pediatr. Nephrol. Berl. Ger.* 27 (2012) 2039–2048, <https://doi.org/10.1007/s00467-012-2175-z>.
- [30] H.D. Kim, H.L. Jang, H.-Y. Ahn, H.K. Lee, J. Park, E.-S. Lee, E.A. Lee, Y.-H. Jeong, D.-G. Kim, K.T. Nam, N.S. Hwang, Biomimetic whitlockite inorganic nanoparticles-mediated in situ remodeling and rapid bone regeneration, *Biomaterials* 112 (2017) 31–43, <https://doi.org/10.1016/j.biomaterials.2016.10.009>.
- [31] Y. Miao, X. Liu, J. Luo, Q. Yang, Y. Chen, Y. Wang, Double-network DNA macroporous hydrogel enables aptamer-directed cell recruitment to accelerate bone healing, *Adv. Sci.* 11 (2023) 2303637, <https://doi.org/10.1002/adv.202303637>.
- [32] T. Kakuta, Y. Takashima, A. Harada, Highly elastic supramolecular hydrogels using host–guest inclusion complexes with cyclodextrins, *Macromolecules* 46 (2013) 4575–4579, <https://doi.org/10.1021/ma400695p>.
- [33] M. Hai, Q. Zhang, Z. Li, M. Cheng, A.J.C. Kuehne, F. Shi, Visualizing polymer diffusion in hydrogel self-healing, *Supramol. Mater* 1 (2022) 100009, <https://doi.org/10.1016/j.supmat.2022.100009>.
- [34] P. Bhattacharya, A. Gopisetty, B.B. Ganesh, J.R. Sheng, B.S. Prabhakar, GM-CSF-induced, bone-marrow-derived dendritic cells can expand natural Tregs and induce adaptive Tregs by different mechanisms, *J. Leukoc. Biol.* 89 (2011) 235–249, <https://doi.org/10.1189/jlb.0310154>.
- [35] W. Chen, J. Ouyang, H. Liu, M. Chen, K. Zeng, J. Sheng, Z. Liu, Y. Han, L. Wang, J. Li, L. Deng, Y. Liu, S. Guo, Black phosphorus nanosheet-based drug delivery system for synergistic photodynamic/photothermal/chemotherapy of cancer, *Adv. Mater.* 29 (2017) 1603864, <https://doi.org/10.1002/adma.201603864>.
- [36] Y. Miao, Y. Chen, J. Luo, X. Liu, Q. Yang, X. Shi, Y. Wang, Black phosphorus nanosheets-enabled DNA hydrogel integrating 3D-printed scaffold for promoting vascularized bone regeneration, *Bioact. Mater.* 21 (2023) 97–109, <https://doi.org/10.1016/j.bioactmat.2022.08.005>.
- [37] M. Kanehisa, M. Araki, S. Goto, M. Hattori, M. Hirakawa, M. Itoh, T. Katayama, S. Kawashima, S. Okuda, T. Tokimatsu, Y. Yamanishi, KEGG for linking genomes to life and the environment, *Nucleic Acids Res.* 36 (2008) D480–D484, <https://doi.org/10.1093/nar/gkm882>.
- [38] H. Uusitalo, J. Rantakokko, M. Ahonen, T. Jämsä, J. Tuukkanen, V.-M. Kähäri, E. Vuorio, H.T. Aro, A metaphyseal defect model of the femur for studies of murine bone healing, *Bone* 28 (2001) 423–429, [https://doi.org/10.1016/S8756-3282\(01\)00406-9](https://doi.org/10.1016/S8756-3282(01)00406-9).